An ESCRT-dependent pathway of Nuclear and Cytoplasmic Spatial PQC is coordinated at Nuclear Vacuolar Junctions

Emily M. Sontag [1,*, †, £], Fabián Morales-Polanco [1,£], Jian-Hua Chen[2], Gerry McDermott[2], Patrick T. Dolan[1,‡], Dan Gestaut[1], Mark A. Le Gros[2,3], Carolyn Larabell[2,3] and Judith Frydman[1,*]

[1] Department of Biology, Stanford University, Stanford, CA 94305, USA

[2] Department of Anatomy, School of Medicine, University of California San Francisco, San Francisco, CA 94158, USA

[3] Molecular Biophysics and Integrated Bioimaging Division, Lawrence Berkeley National Laboratory, Berkeley, CA 94720, USA

[*] Correspondence to: emily.sontag@marquette.edu; jfrydman@stanford.edu,

£ Equal Contribution

† Current address: Department of Biological Sciences, Marquette University, Milwaukee, WI 53233, USA

‡ Current address: Quantitative Virology and Evolution Unit, National Institute of Allergy and Infectious Diseases, Bethesda, MD 20892, USA

Abstract. Spatial sequestration of misfolded proteins is an integral step in the process of cellular Protein Quality Control (PQC). is essential for cellular health. One key PQC strategy relies on spatial sequestration of misfolded proteins into protein inclusions. Herein we define the coordination of nuclear and cytoplasmic spatial PQC. While cytoplasmic misfolded proteins concentrate in a cytoplasmic, perinuclear Juxta Nuclear Quality control (JUNQ) compartment, nuclear misfolded proteins sequester into a perinucleolar IntraNuclear Quality control (INQ) compartment. Particle tracking analysis reveals that INQ and JUNQ converge to localize to face each other across the nuclear envelope at a site proximal to the Nuclear-Vacuolar Junctions (NVJ). Strikingly, this convergence is coordinated by a perinuclear ESCRT pathway involving nuclear envelope-localized ESCRT-II/-III protein Chm7. Indeed, deleting the NVJ or ATPase Vsp4, required for membrane invagination into the vacuole, impairs clearance of inclusions. Furthermore, deleting other ESCRT components led to cytoplasmic accumulation of nuclear misfolded proteins. Our findings uncover an alternative role of perinuclear ESCRT and the nuclear envelope in coordinating spatial PQC and clearance of nuclear and cytoplasmic misfolded proteins into the vacuole.

35 **Introduction**

36 Misfolded proteins can acquire toxic conformations that disrupt essential cellular processes [1-6]
37 leading to a growing number of diseases, including neurodegeneration and cancer [7-10].
38 Accordingly, cellular protein homeostasis (proteostasis) is maintained by a network of chaperones
39 and clearance factors that promote protein quality control (PQC) [11-15]. One fundamental PQC
40 strategy is to spatially sequester misfolded proteins into distinctly localized membrane-less
41 compartments, likely to remove damaging conformers from the cellular milieu and concentrate
42 them for more efficient refolding or clearance through either the ubiquitin-proteasome system
43 (UPS) or endolysosomal pathways [11, 16-18]. Misfolded cytoplasmic proteins partition into distinct
44 inclusions depending on their aggregation state. Insoluble amyloid proteins are sequestered into
45 the Insoluble Protein Deposit (herein the IPOD) [4, 11, 19]. Soluble misfolded proteins are sequestered
46 into small, dynamic, ER-associated structures called Q-bodies [17] which, during sustained stress,
47 coalesce along the endomembrane system [20] into a Juxtanuclear Quality Control compartment
48 (herein the JUNQ). Spatial PQC through the IPOD and JUNQ pathways is evolutionarily
49 conserved and is present in yeast, worms and mammalian cells [11, 19]. Spatial PQC is also observed
50 in the nucleus, as nuclear misfolded proteins are sequestered in a membrane-less intranuclear
51 quality control compartment (herein the INQ), proximal to the nucleolus [18, 21, 22].

52 The relationship and overall coordination between spatial PQC of cytoplasmic and nuclear proteins
53 is not well understood. While many studies showed cytoplasmic misfolded proteins being
54 concentrated into the cytoplasmic JUNQ and cleared through an ER-anchored cytoplasmic UPS
55 pathway [11, 19, 23, 24], it's also been proposed that clearance of cytoplasmic misfolded proteins
56 requires import into the nucleus, whereby the JUNQ would form an inclusion identical to the INQ
57 [18].

58 Given the importance of protein quality control for cell survival and its relevance to understand
59 misfolding diseases, we examined the logic and coordination of spatial PQC for nuclear and
60 cytoplasmic misfolded proteins. We unequivocally demonstrate the cytoplasmic localization of the
61 JUNQ and nuclear localization of the INQ.

62 Of note, the JUNQ and INQ usually home to opposite sides of the nuclear envelope, at a site
63 proximal to NVJ, which facilitates the extrusion of the INQ for clearance into the vacuole in an
64 ESCRT- and VPS4-dependent manner. Here we propose the surprising degree of spatial
65 coordination between nuclear and cytoplasmic PQC inclusions providing an avenue for vacuolar
66 clearance of misfolded proteins.

67 **RESULTS**

68 **Organelle-specific PQC compartments sequester nuclear and cytoplasmic misfolded**
69 **proteins**

70 To define the relationship and interplay between nuclear and cytoplasmic spatial PQC (Fig. 1a),
71 we utilized two validated models of protein misfolding: a temperature-sensitive variant of Firefly
72 Luciferase (herein LuciTs) that misfolds at 37 °C, and the Von Hippel-Lindau (VHL) tumor
73 suppressor, which is constitutively unfolded in yeast cells [25, 26]. We restricted their subcellular
74 localization to either nucleus or cytoplasm by inclusion of a Nuclear Localization Signal (NLS) or
75 a Nuclear Export Signal (NES), respectively. The expression of these PQC substrates was first
76 selectively induced by growth in galactose, and then repressed by glucose addition, which allowed
77 measuring the kinetics of their clearance or spatial PQC (Fig. 1b). As previously described, both
78 NLS- and NES-LuciTs and NLS- and NES-VHL are degraded upon misfolding and are stabilized
79 by proteasomal inhibition with either MG132 or Bortezomib [27] (Extended Data Fig. 1a).

80 To initiate LuciTs misfolding and monitor the fate of the misfolded species, the cells were shifted
81 to 37 °C and evaluated using Time-resolved fluorescence microscopy (Fig. 1b). Under folding-
82 permissive conditions, NLS- and NES-GFP-LuciTs were diffusely localized in the nucleus or
83 cytoplasm, respectively (Time 0, Fig 1 c, d), but following the 37 °C shift, both nuclear (NLS) and
84 cytoplasmic (NES) LuciTs were rapidly concentrated into dynamic puncta in their respective
85 cellular locations (Fig. 1c, d, and Supplemental video 1).

86 Over the course of the experiment, nuclear NLS-LuciTs coalesced into one intranuclear INQ
87 inclusion (Time 30, Fig. 1c). In contrast, cytoplasmic NES-LuciTs puncta coalesced into two
88 cytoplasmic inclusions, corresponding to the JUNQ and IPOD (Time 30, Fig. 1d), as previously
89 observed for Ubc9Ts and VHL [11]. Of note, the NLS- and NES- LuciTs variants formed inclusions
90 in both absence or presence of proteasome inhibitor MG132 (Figure 1c, d), indicating that spatial
91 sequestration into PQC compartments is not a consequence of proteasomal inhibition.

92 We used structured illumination (SIM) super-resolution microscopy to better define the nuclear
93 and cytoplasmic location and morphology of these PQC inclusions. Cells expressing LuciTs
94 variants were incubated for 2 hrs at 37 °C, while cells expressing VHL variants were grown and
95 fixed at both 30 and 37 °C. The nuclear envelope was visualized by immunostaining of nuclear
96 pore protein Nsp1 (Nups, yellow) and DNA was visualized using Hoechst (blue) (Fig. 1e-h). The
97 INQ, formed by nuclear misfolded protein, localized inside the nucleus in a pocket between the
98 nuclear envelope (delineated by Nups) and the DNA (Fig. 1e and Supplemental video 2 for NLS-
99 LuciTs at 37 °C, Fig. 1f for NLS-VHL at 30 °C Extended Data Fig. 1c for NLS-VHL at 37 °C).
100 Line intensity profile analyses confirmed the intranuclear localization of this INQ (Fig. 1e, f,
101 Extended Data Fig. 1c). Importantly, SIM and line intensity profile analyses unequivocally
102 established that the PQC inclusions formed by cytoplasmic misfolded proteins NES-LuciTs and

103 NES-VHL reside outside of the nucleus: one inclusion is adjacent to the nuclear envelope as
104 expected for the JUNQ, while the other inclusion is closer to the cell periphery as expected for the
105 IPOD (Fig. 1g-h, Supplemental video 2, Extended Data Fig. 1d). Similar results were obtained
106 with NLS- and NES-VHL at both 30 °C and 37 °C indicating PQC inclusion localization is not
107 temperature-dependent (Extended Data Fig. 1c-d). Consistent with their distinct localization,
108 cytoplasmic and nuclear misfolded variants also exhibit differential toxicity to cells; cytoplasmic
109 misfolded proteins were slightly more toxic, albeit less so than a polyglutamine expanded exon1
110 variant of Huntingtin (herein mHTT) associated with Huntington's disease (Extended Data Fig.
111 1b). The increased NES-LuciTs toxicity, only observed at 37 °C when it is misfolded, may be
112 associated with the slower clearance kinetics of the cytoplasmic misfolded variant, which is much
113 slower than that of misfolded NLS-LuciTs (Extended Data Fig. 1a).

114 We conclude that nuclear and cytoplasmic misfolded proteins are spatially sequestered in PQC
115 inclusions located in their cognate compartment, yielding the INQ and JUNQ respectively.
116 Together with findings that UPS degrades nuclear and cytoplasmic misfolded proteins through
117 different chaperones and ubiquitination enzymes [27], our data indicate that the nucleus and the
118 cytoplasm have compartment specific PQC machineries.
119

120 **Proteasome inhibition disrupts nucleocytoplasmic transport**

121 Most commonly used PQC reporters (e.g. Ubc9Ts, VHL, Cpy*, and Luciferase, etc.), are smaller
122 than the 200 kDa nuclear permeability barrier [28-30]. To examine if passive diffusion across nuclear
123 pores could lead cytoplasmic misfolded proteins to form intranuclear inclusions, we utilized
124 temperature-sensitive variant of Ubc9 (Ubc9Ts) [11, 17, 18]. Upon Ubc9Ts unfolding at 37 °C for 2
125 hours under conditions where the proteasome is active, SIM super-resolution microscopy showed

126 Ubc9Ts is sequestered exclusively in two cytoplasmic compartments – the perinuclear JUNQ,
127 clearly outside the nuclear pore boundary and the IPOD in the cell periphery (Fig. 2a,
128 Supplemental Video 3). When cells were treated at 37 °C for 2 hr with added proteasome inhibitor
129 MG132, Ubc9Ts also formed the two cytoplasmic inclusions as above, but some cells (around
130 13%) had an additional Ubc9Ts inclusion inside the nucleus (Fig. 2b, Extended Data Fig. 2a,
131 Supplemental Video 3). Of note, MG132 treatment led to a general increase in cells containing
132 inclusions in both nucleus and cytoplasm (Extended Data Fig. 2a). Similar results were obtained
133 for another PQC substrate, VHL (Extended Data Fig. 2b). Interestingly, line intensity profile
134 analyses of both Ubc9Ts and VHL showed that their nuclear INQ and cytoplasmic JUNQ
135 inclusions formed in close proximity but separated by nuclear pores (Fig. 2b), These results
136 confirmed that cytoplasmic proteins that can passively diffuse into the nucleus, primarily form
137 cytoplasmic inclusions, but also suggested that absent an exogenous NLS or NES localization tag,
138 they can form an additional distinct nuclear INQ in a small fraction of cells under conditions of
139 proteasome inhibition.

140 To reconcile the finding that spatial sequestration into a nuclear or a cytoplasmic PQC inclusion
141 depends on a misfolded protein's subcellular location when they misfold (Fig. 1a) with the fact
142 that MG132 leads to a small fraction of cells having a nuclear Ubc9Ts and VHL inclusion, we
143 hypothesized that prolonged proteasome inhibition may alter nucleocytoplasmic trafficking and
144 decrease protein export from the nucleus. Indeed, toxic misfolded proteins that affect proteostasis,
145 such as the polyglutamine expanded mHTT, can affect nucleocytoplasmic transport [31, 32].

146 We examined the effect of MG132 on nucleocytoplasmic transport using an NLS- and NES-tagged
147 shuttling GFP (sGFP) that migrates between the nucleus and cytoplasm [31, 33] (Fig. 2c, d). As
148 described, toxic mHTT expression caused sGFP to be retained in the nucleus (Fig. 2c, d). Of note,

149 proteasome inhibition with MG132 caused sGFP nuclear retention to the same extent as mHTT
150 (Fig. 2c, d). This experiment was performed in leptomycin B-sensitive *crm*^{T539C} cells, which
151 permitted the use of leptomycin B (LMB) as a positive control for blocked nuclear export (Fig. 2c,
152 d), but similar results were obtained using WT BY4741 yeast cells (not shown).

153 Our finding that proteasome inhibition impairs nuclear export similar to expression of toxic mHTT
154 may explain the increased retention of misfolded protein Ubc9Ts in the nucleus. Future studies
155 should examine the basis for reducing nuclear export when proteostasis is impaired [31, 34, 35].
156 To directly examine if clearance of cytoplasmic proteins requires their import to the nucleus, we
157 examined Ubc9Ts clearance in *nup116-5 yeast* cells that. carry a temperature-sensitive mutation
158 in the nuclear pore complex (NPC) protein Nup116. At 37 °C, the *nup116-5* mutation seals nuclear
159 pores over the cytoplasmic face of NPCs blocking any transport into and out of the nucleus [36] (Fig.
160 2f, *i*). WT and *nup116-5* cells expressing Ubc9Ts were shifted to 37 °C for 1 hour prior to the
161 glucose-repression to ensure nuclear pores become completely sealed before start measuring
162 Ubc9Ts clearance (Figure. 2e, *ii*). If degradation of misfolded Ubc9Ts requires import into the
163 nucleus, it should be abrogated in *nup116-5* cells at 37 °C. We did not observe any significant
164 differences in the rate and the extent of Ubc9Ts degradation in *nup116-5* cells, suggesting that
165 transport into the nucleus is not required for its clearance (Figure. 2f, *ii-iii*; Extended Data Fig. 2c).

166 We next examined whether nuclear proteasomes participate in the clearance of a cytoplasmic
167 misfolded protein. To this end, we used *sts1-2* yeast cells that carry a mutation in Sts1, a protein
168 required for import of proteasomes into the nucleus and facilitate the degradation of nuclear
169 proteins. At 37 °C, nuclear localization of proteasomes is lost in *sts1-2* cells [37-40] (Fig. 2g panel *i*).
170 However, preventing nuclear localization of proteasomes had no effect on the clearance of
171 misfolded Ubc9Ts, consistent with cytoplasmic degradation (Fig. 2g, panel *ii-iii*; Extended Data

172 Fig. 2d). Therefore, together these experiments suggest that import of misfolded proteins and
173 proteosomes into the nucleus is dispensable to degrade misfolded Ubc9Ts.

174

175 **INQ and JUNQ home into adjoined locations on opposite sides of the nuclear envelope**

176 Given that nuclear and cytoplasmic Ubc9Ts inclusions in cells treated with MG132 appeared to
177 localize to opposite sides of the nuclear envelope (Fig. 2b), we next sought to define the spatial
178 relationship between INQ and JUNQ in live cells.

179 To this extent, NLS- LuciTs and NES- LuciTs were co-expressed in WT yeast cells at 25 °C for 6
180 hr before repressing their synthesis with glucose. Cells were then shifted to 37 °C to unfold both
181 proteins simultaneously, and live cell time-lapse fluorescence microscopy and particle tracking
182 analysis were performed to monitor inclusion formation in real-time (Fig. 3a, b; Extended Data
183 Fig. 3a; Supplemental Videos 4, 5). Spatial sequestration of the NLS- and NES- misfolded proteins
184 into motile condensates occurred with similar kinetics independently in the nucleus and the
185 cytoplasm. We then noticed that in some cells, the puncta moved dynamically toward each other,
186 with both nuclear and cytoplasmic inclusions converging on a specific location that was proximal
187 to the nuclear envelope (Fig. 3a). Of note, even after homing to this location, the two inclusions
188 remain distinct and separated; however, they co-migrated around the nuclear periphery as if
189 tethered to each other across the nuclear envelope. Particle tracking analyses measuring the
190 location and distance of NLS- and NES-LuciTs inclusions in 2D space showed the nuclear and
191 cytoplasmic inclusions homed into adjoining locations between 10 and 20 minutes after shifting
192 to 37 °C, and then continued moving in a coordinated fashion throughout the duration of the
193 imaging experiment (Fig. 3b; Extended Data Fig. 3a; Supplemental video 5). While the distance
194 between these two inclusions decreased rapidly during homing, once they came together they

195 maintained a largely stable short distance, suggestive of a tether, throughout their co-migration for
196 the remainder of the experiment. Similar results were obtained if the fluorescent markers in NLS-
197 and NES-LuciTs were reversed (not shown) as well as for NLS- and NES-VHL (Extended Data
198 Fig. 3b). These observations, supporting our findings with Ubc9Ts, suggest a novel mechanism
199 coordinating convergence of nuclear and cytoplasmic PQC compartments.

200 We confirmed the spatial relationship between the INQ and the JUNQ using SIM super-resolution
201 microscopy. Cells co-expressing NLS-LuciTs and NES-LuciTs were incubated at 37 °C for 2 hrs
202 and then fixed and immunostained to detect nuclear pores (Fig. 3c). SIM combined with line
203 intensity profile analysis confirmed the INQ and JUNQ adjoined each other on opposite sides of
204 the nuclear envelope, separated by the nuclear pores (Fig. 3c; Supplemental video 6).

205

206 **Nuclear pores play a role in INQ-JUNQ convergence at the nuclear periphery**

207 To understand the nature of the signal bringing together the INQ and JUNQ, we examined their
208 subcellular co-localization with specific nuclear and perinuclear structures. The INQ was near the
209 nucleolus but not in direct contact, suggesting the nucleolus is not driving this homing mechanism
210 (Extended Data Fig. 3c). We also examined the relationship of the INQ-JUNQ homing signal with
211 two complexes that localize at a defined perinuclear location: the spindle pole body (SPB) and the
212 LINC complex, both of which contain protein Mps3 spanning both layers of the nuclear envelope
213 (Extended Data Fig. 3d). Co-staining with Mps3 showed neither SPB nor LINC co-localize with
214 the INQ-JUNQ perinuclear site, suggesting they do not participate in the INQ-JUNQ homing
215 mechanism (Extended Data Fig. 3d).

216 To investigate the role of nuclear pores in INQ/JUNQ homing, we exploited the finding that
217 deletion of nuclear pore protein Nup120 causes nuclear pores to remain functional but become
218 clustered [41, 42]. We thus compared INQ and JUNQ formation and localization in WT and *nup120Δ*
219 cells. In *nup120Δ* cells, the JUNQ always forms next to the clustered nuclear pores (Fig. 3d, panel
220 *i*) while the INQ did not localize proximal to the nuclear pores, but instead was found anywhere
221 within the nucleus (Fig. 3d, panel *ii*). Surprisingly, if we co-expressed NLS- and NES-LuciTs in
222 *nup120Δ* cells, the INQ now homed to the clustered nuclear pores opposite the JUNQ (Fig. 3d,
223 panel *iii*). This finding suggests formation of the JUNQ at the cytoplasmic side of the nuclear pores
224 communicates a signal for INQ recruitment to this location (Fig. 3e).

225 We then reasoned that the intrinsically disordered phenylalanine-glycine (FG) repeats in the
226 central nuclear pore channel, which form hydrogels capable of amyloid-like interactions [43], could
227 facilitate INQ-JUNQ homing. Using live-cell time-lapse microscopy we examined the localization
228 of the INQ and JUNQ in *nupΔFG* cells, carrying deletions in the FG repeat tracts of six nuclear
229 pore proteins that removes approximately 70% of the FG content from the nuclear pore [44]. We
230 found that the INQ and JUNQ still localized to the same perinuclear location in *nupΔFG* cells
231 suggesting the high percentage of FG-repeats are dispensable for homing (Extended Data Fig. 3e).
232 Although, we cannot exclude the possibility that that the remaining 30% of FG content is still
233 sufficient to direct convergence of the INQ and JUNQ to the proximity of nuclear pores.

234 **Cryo-soft X-ray tomography reveals the architecture of PQC inclusions in intact cells**

235 To examine the native cellular context of PQC compartments, we used cryogenic Soft X-ray
236 Tomography (cryo-SXT), a synchrotron-based imaging approach that visualizes and quantifies the
237 ultrastructure of intact, unstained, cryo-preserved cells (Fig. 4a, Extended Data Fig. 4a, b) [45, 46].
238 This method uses the characteristic linear absorption of X-rays by different subcellular organelles

239 to produce projection images of cellular ultrastructure to a few tens nanometers of spatial
240 resolution [47]. To derive the information content needed to study misfolded protein inclusions we
241 initially used cryo-SXT in correlation with cryo-fluorescence microscopy (Fig. 4b,i). The ability
242 to absorb X-rays varies with the type and density of biomolecules present in different
243 compartments, yielding characteristic linear absorption coefficients (LAC) (Fig. 4b, ii) [48-50]. Since
244 chaperone Hsp104 localizes to both the JUNQ and IPOD upon heat shock, while aggregation-
245 prone mHTT only localizes to the IPOD [11, 20], we visualized these PQC compartments by
246 expressing mHTT-ChFP in cells with chromosomally tagged HSP104-GFP [51]. The inclusions
247 were formed by 1 hr incubation at 37 °C and cells were flash frozen in capillary tubes and directly
248 imaged using cryo-SXT correlated with cryo-fluorescence microscopy (Fig. 4b, i). The LAC
249 values were used to identify the exact location of specific compartments and organelles in X-ray
250 tomograms of intact frozen yeast cells (Fig. 4b, ii), yielding a 3D reconstruction of the PQC
251 inclusions in the context of cellular architecture (Fig. 4c, Supplemental Video 7). Cryo-
252 fluorescence identified the PQC compartments, with Hsp104-only marking the JUNQ and co-
253 localized Hsp104 and mHTT marking the IPOD. This analysis revealed that protein inclusions
254 have a characteristic LAC that can be used to examine their location and size without the need of
255 fluorescence microscopy. Of note, this correlated fluorescence-cryo-SXT analyses confirmed both
256 the JUNQ and the IPOD are cytoplasmic, as previously described (Fig. 4c, Supplemental Video 7
257 and [11]).

258 We next used cryo-SXT to directly detect inclusions formed by NLS- and NES-LuciTs at 37 °C
259 through their characteristic LAC values. NES-LuciTs formed small, cytoplasmic, punctate Q-
260 bodies that could be seen congregating at a cytoplasmic, juxtanuclear location to form the JUNQ
261 (Fig. 4d, Supplemental Video 8). Thus, cryo-SXT indicates the JUNQ is not the homogeneous

262 large compartment suggested by diffraction-limited fluorescence imaging, but rather consists of
263 multiple dense "cores" that resemble Q-bodies. This conclusion, also supported by the irregular
264 JUNQ morphology in SIM and cryo-EM imaging (Fig. 1, Fig 5 and [52]), suggests the JUNQ is in
265 fact a collection of Q-bodies that congregate at a perinuclear location proximal to the nuclear
266 envelope (Fig. 4d, inset *ii*; Supplemental video 8).

267 Cryo-SXT analysis also revealed a link between cytoplasmic PQC and mitochondria. Individual
268 Q-bodies can associate with the surface of mitochondria (Fig. 4e) and the JUNQ and IPOD appear
269 surrounded by a mitochondrial cage (Fig. 4d, *i*). Confocal fluorescence microscopy of cells
270 expressing mito-GFP supported the mitochondrial association with Q-bodies (Extended Data Fig.
271 4d). However, PQC compartments still formed in cells with disruptions in mitochondrial fission
272 or fusion (Extended Data Fig. 4e) indicating mitochondrial structure does not direct PQC
273 compartment formation. Since previous studies placed Q-bodies on the ER membrane [17, 20], which
274 cannot be visualized by cryo-SXT, it is possible that Q-bodies are proximal to ER-mitochondrial
275 contact sites. Alternatively, the proximity to mitochondria may serve to place energy-intensive
276 PQC compartments in areas of the cell enriched in ATP production [53].

277 Cryo-SXT also confirmed that the intranuclear INQ is distinct from but resides near the nucleolus
278 (Fig. 4g). This conclusion is supported by confocal fluorescence microscopy with nucleolar protein
279 Nsr1 (Extended Data Fig. 3c, 4c and [18, 31]). The proximity of the nucleolus to the INQ is consistent
280 with the nucleolus' role in nuclear folding and assembly [21, 54-56] and suggest a possible link to the
281 INQ's function in nuclear PQC [54, 57].

282 Strikingly, our cryo-SXT imaging revealed an unexpected link of both INQ and JUNQ with the
283 vacuole. The entire JUNQ site was surrounded by nuclear-vacuolar inter-organelle contact sites,
284 suggesting the idea that the vacuole promotes JUNQ clearance (Figure. 4f, red arrows;

285 Supplemental Video 8). Remarkably, Q-bodies in the JUNQ area were nestled within
286 invaginations in the vacuolar membrane, further suggestive of direct vacuolar engulfment (Figure.
287 4f, blue arrows; Supplemental Video 8). Of note, the INQ was also proximal to the vacuolar side
288 of the nucleus, indicating both INQ and JUNQ are steered to the vicinity of nuclear-vacuolar
289 contact sites (Fig. 4g). The nucleus-vacuole contact sites are formed by a tethering complex
290 between nuclear Nvj1 and vacuolar Vac8 called the Nuclear-Vacuolar Junction (NVJ) (Fig. 4h and
291 [58]). Consistent with the idea that the INQ and JUNQ converge to the vicinity of NVJs, all nuclear
292 pores in *nup120*Δ cells cluster at the vacuole-contacting side of the nucleus [42].

293

294 **Nuclear-Vacuolar Junctions facilitate clearance of JUNQ and INQ**

295 The role of NVJs remains poorly understood, but it has been implicated in lipid droplet biogenesis,
296 nuclear envelope autophagy, amino acid metabolism and a specialized form of autophagy called
297 Piecemeal Microautophagy of the Nucleus (PMN), where portions of the nucleus invaginate into
298 the vacuole [59-64]. We assessed the co-localization of the JUNQ and the NVJ by expressing NES-
299 LuciTs or Ubc9Ts in cells carrying a chromosomally tagged Nvj1-GFP [51]. Live-cell time-lapse
300 microscopy revealed transient and dynamic interactions between JUNQ and Nvj1, whereby both
301 puncta came in contact and then separated (Fig. 5a; Extended Data Fig. 5a; e.g. observe 9 min to
302 11 min in Supplemental Video 9).

303 The architecture of perinuclear spatial PQC and the close association of the INQ and JUNQ in
304 relation to the NVJ were next examined using SIM super-resolution microscopy (Fig. 5b-e;
305 Supplemental Videos 10, 11). The NVJ, visualized via Nvj1 imaging, forms a basket-shaped
306 structure contouring the Nuclear Envelope and connected to the vacuole (Fig. 5d). In these super-
307 resolution images, the JUNQ, visualized by NES-LuciTs, was proximal to the cytoplasmic side of

308 the NVJ as observed by Cryo-SXT (Fig. 5b). Of note, the Q-body "assembly" substructure of the
309 JUNQ was evident in these images. On the other hand, the nuclear INQ, visualized by NLS-
310 LuciTs, was nestled between the concave nuclear side of the NVJ and the nuclear DNA (Fig. 5c).
311 Strikingly, we were able to observe in some cells the INQ being extruded through the NVJ to enter
312 the vacuole (Fig. 5e; Supplemental Video 12). These experiments suggest dynamic tethering of
313 the INQ and JUNQ to the NVJ vicinity account for the homing and slight fluctuations in distance
314 between these inclusions observed in particle tracking experiments in Fig. 3.

315 We then tested if NVJs play a role in INQ and JUNQ clearance using *nvj1Δ* or *vac8Δ* yeast cells.
316 Live-cell time course analyses provided an unexpected insight into NVJ function. In *nvj1Δ* cells,
317 nuclear and diffuse NLS-LuciTs formed an initial nuclear inclusion, but during the time-course,
318 some cells showed the INQ being egressed from the nucleus into the cytoplasm (Fig. 5f).
319 Strikingly, some of the egressed NLS-LuciTs puncta ended up co-localizing with NES-LuciTs
320 (Fig. 5f, inset; Supplemental Video 13; white arrowheads). Similar results were obtained when
321 cycloheximide was added together to the temperature shift (Extended Data Fig. 5b) to ensure all
322 the NLS-LuciTs is in the nucleus. We observed NLS-LuciTs extruded from the nucleus in the
323 *njv1*Δ but not the WT cells, confirming NVJ disruption leads to nuclear extrusion of the INQ.
324 Confocal microscopy in *nvj1Δ* and *vac8Δ* cells confirmed that NVJ disruption led to extrusion of
325 nuclear NLS-LuciTs into the cytosol, where it ended up co-localizing with NES-LuciTs puncta
326 (Fig. 5g; white arrowheads). Of note, deleting the NJVs does not disrupt INQ and JUNQ
327 convergence, as the INQ and JUNQ are still juxtaposed in both *nvj1Δ* and *vac8Δ* cells (Fig. 5g).

328 We next examined if deletion of the NVJ affects clearance of PQC inclusions. Indeed, we observed
329 dramatic increases in the fraction of cells containing NLS and NES-LuciTs inclusions in
330 *nvj1Δ* and *vac8Δ* cells compared to WT cells (Fig. 5h, panels *i, ii*; Extended Data Fig. 5c,d), as

331 well as the levels of misfolded protein (Extended Data Fig. 5e). MG132 addition led to a
332 synergistic enhancement in the number of cells with NES-LuciTs inclusions, suggesting the NVJ
333 and the proteasome represent distinct cytoplasmic clearance pathways (Extended Data Fig. 5c).
334 The synergy effect for NLS-LuciTs inclusions was marginal, perhaps because the higher fraction
335 of cells with INQs poses a ceiling effect to our measurements, or because the NVJ plays a greater
336 role in the clearance of nuclear protein inclusions (Extended Data Fig. 5b). Further supporting a
337 role in misfolded protein clearance, NVJ deletion sensitizes cells to proteotoxic stress (Fig. 5i).
338 Both *nvj1Δ* and *vac8Δ* cells are sensitive to treatment with proline analog AZC, which induces
339 widespread misfolding of newly translated proteins (Fig. 5i).

340 The findings that the INQ and JUNQ converge on nuclear-vacuolar contact sites and that the NVJ
341 is required for efficient clearance of nuclear and cytoplasmic inclusions define the NVJ as a
342 cellular center for spatial protein quality control.

343 **ESCRT proteins are required for INQ-JUNQ homing and clearance at the vicinity of NVJs**

344 The relationship observed between spatial PQC and the nuclear-vacuolar contact sites led us to
345 examine the role of the perinuclear ESCRT-II/III protein Chm7 (CHMP7 in mammals) which
346 participates in nuclear envelope sealing and nuclear pore quality control [65-67] (Fig. 6a, *i*). In yeast,
347 Chm7 is normally diffuse throughout the cytoplasm (Extended Data Fig. 6a),and becomes
348 associated with a unique site in the nuclear envelope upon activation.

349 The active conformation of Chm7 can be induced by deleting auto-inhibitory helices in the
350 ESCRT-III domain [herein $Chm7_{OPEN}$] [67, 68]. Strikingly, activated $Chm7_{OPEN}$ localized to a single
351 site in the nuclear envelope in close proximity with both INQ and JUNQ (Fig. 6a, *ii*), suggesting
352 that this perinuclear ESCRT protein marks the site of INQ and JUNQ convergence for vacuolar
353 delivery.

354 We next examined the impact the absence of Chm7 had on INQ and JUNQ subcellular
355 localization. In *chm7Δ* yeast cells, both INQ and JUNQ still formed and migrated to the
356 perinuclear region, but they no longer converged to the same location (Fig. 6b), suggesting a novel
357 role for the Chm7 ESCRT protein as recruiting nuclear and cytoplasmic PQC compartments to the
358 proper location on the nuclear envelope for further clearance for terminal sequestration.

359 Since Chm7 is an ESCRT II/III protein, we next examined the role of other ESCRT proteins in
360 spatial PQC: the ESCRT-I Vps23 and the membrane bound phosphatidylinositol 3-kinase (PI3K)
361 Vps34-Vps15. Vps23 is a component of the ESCRT-I complex that binds to ubiquitinated cargo
362 proteins and mediates their vacuolar transport [69-71]. The Vps34-Vps15 complex is essential for
363 protein sorting to the vacuole and has been shown to localize to nuclear pores at NVJs [72-75]. We
364 co-expressed NLS- and NES-LuciTs in WT, *vps23Δ*, *vps34Δ*, *and vps15Δ* cells, and followed their
365 fate by inducing unfolding at 37 °C. We observed INQ and JUNQ formation in both WT and
366 ESCRT mutants. However, the spatial relationship between INQ and JUNQ was disrupted in all
367 three ESCRT mutants, which showed similar aberrant phenotypes (Fig. 6c, Extended Data Fig.
368 6b). We observed that in most of the ESCRT mutant cells, the INQ and JUNQ were no longer
369 homed and/or displayed cytoplasmic egress of the INQ (Fig. 6c, Extended Data Fig. 6b).
370 Strikingly, in a subset of *vps23Δ* and *vps34Δ* cells we observed a possible intermediate of the
371 nuclear egress of the INQ, whereby the NLS-LuciTs inclusion was fully enveloped by the nuclear
372 membrane in what appears to be a budding event (Fig. 6c, Extended Data Fig. 6b). These data
373 suggest that the ESCRT pathway plays a role in homing of INQ and JUNQ to the NVJ and in the
374 extrusion of the INQ, likely to mediate vacuolar delivery and clearance. When this process is
375 perturbed, as in the NVJ deletion or the ESCRT mutants, the INQ can bud into the cytoplasm.

376 Our analyses suggest the NVJ tethers nuclear-vacuolar contacts whereby a perinuclear ESCRT
377 pathway promotes vacuolar clearance of the INQ and JUNQ. Since vacuolar engulfment often
378 requires the AAA-ATPase Vps4, which functions by disassembling ESCRT-III complexes [76, 77]
379 (Fig. 6d), we next examined the effect of deleting Vps4 on INQ and JUNQ clearance as described
380 above. The *vps4*Δ cells contained more NLS- and NES-LuciTs inclusions than WT controls (Fig.
381 6e) indicating that Vps4 is required for clearance of both INQ and JUNQ. Strikingly, NLS-LuciTs
382 also egressed into the cytoplasm in some *vps4*Δ cells (Fig. 6f), indicating Vps4 mediates INQ
383 budding into the vacuole. Together, these results indicate that nuclear misfolded proteins
384 sequestered in the INQ are homed to the nuclear side of NVJ to be extruded out of the nucleus and
385 into the vacuole in an ESCRT family protein-dependent manner.

386 **Vacuolar clearance of INQ and JUNQ**

387 To directly examine vacuolar targeting of nuclear and cytoplasmic inclusions in yeast we utilized
388 the pH sensitive protein sensor Keima (Fig. 7a). Keima has a fixed emission spectrum that does
389 not change with pH with a maximum peak at 620 nm [78] , whilst its excitation spectrum changes
390 according to pH. A short wavelength spectrum with a maximum of 440 nm is predominant in a
391 neutral cellular environment, while a longer wavelength of 586 nm is predominant in an acidic
392 environment [78, 79]. Considering that Keima in yeast has been reported to have a weak emission
393 intensity, and to be easily bleached [79], we N-terminally tagged NLS- and NES-LuciTs with two
394 consecutive Keima moieties (herein 2xKeima-LuciTS; Fig. 7a, b, schematic). In the folded state,
395 both NLS-LuciTS and NES-LuciTS proteins were diffusely located in the nucleus and the
396 cytoplasm respectively with 620 nm emission observed mostly under 404 nm excitation
397 wavelength characteristic of a neutral pH environment. Upon misfolding at 37 °C, both NLS-
398 LuciTs-Keima and NES-LuciTs-Keima formed the nuclear INQ and cytoplasmic JUNQ

399 respectively maintaining maximum emission after 404 nm excitation, suggesting that inclusion
400 formation takes place initially at their respective subcellular location on a neutral pH environment.

401 However, upon continued incubation at 37 °C, emission at 620 nm following 558 nm excitation
402 starts appearing for both inclusions, characteristic of an acidic environment like the vacuole (Fig.
403 7c, d, Extended Data Fig. 7a, b). The kinetics of acidification of the JUNQ seemed to be slower
404 than for the INQ, consistent with its slower clearance kinetics (Extended Data Fig. 1a). For the
405 INQ, the red shift appears to initiate at the nuclear envelope boundary with an elongated structure
406 observed extending from the inclusion and entering the vacuole (Fig. 7c). The slower degradation
407 kinetics of the JUNQ coupled with the low quantum yield and quick photobleaching of Keima
408 precluded continuous live-imaging of the JUNQ, but an imaging time course of different regions
409 on the same slide showed multiple red foci arising proximal to the JUNQ (Fig. 7d; Extended Data
410 Fig. 7a-b). Of note, these experiments were carried out under conditions of ongoing proteasome
411 degradation indicating vacuolar targeting occurs in parallel to UPS-mediated clearance of
412 misfolded proteins.

413 The contribution of vacuolar and proteasomal pathways in the clearance of misfolded nuclear and
414 cytoplasmic proteins was independently assessed using immunoblot analyses (Fig. 7e-f). Briefly,
415 GFP-tagged NLS- and NES-LuciTs were expressed under permissive conditions, followed by
416 glucose repression, as described in Fig 1. Following unfolding, the levels of remaining luciferase
417 were examined after 2 and 4 hrs at 37 °C by immunoblot analyses probing for the GFP moiety.
418 The contribution of proteasomal clearance was assessed by addition of 50 uM Bortezomib [27, 80]
419 (Bz) at T=0, while the contribution of vacuolar clearance was assessed using cells deleted for Pep4,
420 required for maturation of vacuolar proteinases, supplemented with 1mM PMSF to inhibit vacuolar
421 serine proteases [81]. As expected, the levels of full length nuclear and cytoplasmic luciferase

422 decreased as a function of time, and were partially stabilized by proteasomal inhibition (Figure 7
423 e,f; Extended Data Fig. 7c-e). Inhibition of vacuolar proteases in the *pep4*Δ cells stabilized both
424 the nuclear and cytoplasmic full-length prote[82, 83]ins (Figure 7c-e; Extended Data Fig. 7c,e).
425 Interestingly, we also observed a range of GFP-positive degradation products in the WT and +Bz
426 cells that disappear when the vacuolar proteases were inhibited (Figure 7g), which is a hallmark
427 of vacuolar targeting of GFP-tagged proteins [62, 63, 81, 84-87]. Quantification of the intensity of
428 degradation fragments relative to initial full-length protein confirmed the reduction in clearance
429 when vacuolar proteases are inhibited (Fig. 7g). A longer exposure reveals fewer bands and a
430 completely different banding pattern between WT and protease inhibited cells (Extended Data Fig.
431 7c).

432 The finding that inhibiting vacuolar proteases stabilizes NLS-LuciTs supports the existence of a
433 pathway to transfer nuclear PQC substrates to the vacuole. To independently corroborate this, we
434 next carried out live-cell time resolveimaging of the dynamic clearance of the INQ through the
435 vacuole (Fig. 7g). The INQ was visualized via NLS-LuciTs-GFP and the vacuole using the styryl
436 dye FM4-64 commonly used to visualize endocytosis and vacuolar membrane dynamics [88] (Fig.
437 7g; Supplemental Video 14). Since GFP fluorescence is quenched by the acidic vacuolar
438 environment, NLS-LuciTS[82, 83, 89, 90] (Fig. 7g; supplemental video 14; Extended Data Fig. 7d). In
439 WT cells, the INQ is opposed to the vacuole at the start of the time course and appears to be pulled
440 into the vacuole as a function of time. Fascinatingly, when the nuclear-vacuolar contact is
441 disrupted in *nvj1*Δ, the INQ is unable to interact with and enter the vacuole and moves dynamically
442 without becoming degraded (Fig. 7g, second row; Supplemental Video 15). Strikingly, in the vast
443 majority of *vps4*Δ cells, the INQ looks still proximal to the vacuole but does not get cleared,

444 supporting a role for Vps4-mediated membrane scission for INQ vacuolar engulfment (Fig 7g,
445 third row; Supplemental Video 16).

446 **DISCUSSION**

447 Spatial sequestration of misfolded proteins into membrane-less inclusions is an integral step in
448 PQC. Here, we demonstrate that the cytoplasm and the nucleus form distinct compartments of
449 spatial PQC and that both follow a path for clearance to the vacuole when the proteasome is
450 overburdened. We observed that, while cytoplasmic misfolded proteins are sequestered into a
451 cytoplasmic perinuclear JUNQ compartment, the nuclear misfolded proteins are sequestered into
452 a nuclear peri-nucleolar INQ compartment. Strikingly, we find the JUNQ and INQ sometimes
453 converged to face each other across the nuclear envelope at a site proximal to the Nuclear-Vacuolar
454 Junctions (NVJ). The homing process is coordinated by nuclear pores and a perinuclear ESCRT
455 pathway involving ESCRT II/III protein Chm7 likely to undergo Vps4-dependent vacuolar
456 degradation (See integrative model in **Figure 8)**. Our experiments provide insights into logic of
457 spatial PQC. Upon misfolding, it is well known that misfolded proteins are cleared by independent
458 pathways in the nucleus and cytoplasm [27]. We show that under situations of limited proteosomal
459 activity, nuclear and cytoplasmically localized proteins form protein inclusions as a means to
460 provide an alternate specific clearance pathway. Our data support the literature demonstrating
461 compartment specific clearance [27, 91]. Previous work from our lab has shown that there are distinct
462 ubiquitin linkages for the nucleus and cytoplasm [27]. Here we show that in addition to these distinct
463 proteostasis machineries for the UPS, the nucleus and cytoplasm form inclusions independently
464 and communicate to facilitate clearance through the vacuole.

465

466 Our experiments also demonstrated that the JUNQ is a conglomerate of Q-bodies as seen in [52, 92].
467 This finding is particularly intriguing as it alludes to these membrane-less inclusions behaving like
468 liquid-liquid phase separated droplets (Q-bodies) coming together to form a larger structure
469 (JUNQ). Notably, the Q-bodies were visible in the cryo-SXT data (Figure 4d-f) and had a distinct
470 linear absorption coefficient (Figure 4b) to allow them to be visualized without further
471 manipulation such as staining. This finding makes cryo-SXT a particularly useful tool for
472 examining phase separated material in the future.

473 Many of our experiments were done in the absence of proteasome inhibitor (Figures 1c-d, 2a, c-g,
474 5h, 7c-g). These experiments are critical for our understanding of sequestration as part of normal
475 PQC. Both the Keima (Figure 7c, d) and Western blot data from *vps4Δ* cells (Figure 7e-g) confirm
476 that the vacuolar protein clearance mechanism is active even when the proteasome is active (Figure
477 7c-g). This indicates that clearance through the vacuole is not only activated during times of
478 proteasomal stress as a compensatory mechanism for the loss of proteasome activity.

479 We observe convergence of INQ and JUNQ to the nuclear-vacuolar region (Figure 3a-c). We posit
480 this could represent a way to provide an important alternative clearance route upon conditions of
481 proteasome overload. In particular, it offers a path to clear the nuclear compartment from
482 misfolded proteins through extrusion of the INQ from the nucleus via the NVJ (Figure 5c-f). As
483 such, we observe a strong interaction between NVJ1 and the INQ by SIM and 3D reconstruction
484 (Figure 5c, e). The physical tether provided by NVJs mediates engulfment of regions of the nuclear
485 membrane into the vacuole. A similar mechanism mediating egress of the INQ into the vacuole
486 could explain how NVJ disruption leads to INQ extrusion into the cytoplasm.

487 Previous studies described a perinuclear ESCRT-II/III protein Chm7 (CHMP7 in mammals),
488 linked to remodeling nuclear envelopes [65], clearance of misassembled nuclear pores [66], egress of

489 herpes virus from the nucleus to the cytosol [93], as well as nuclear envelope sealing and nuclear
490 pore quality control [67]. We hypothesized that Chm7 participated in the homing of the INQ and the
491 JUNQ. In yeast, Chm7 is normally diffuse throughout the cytoplasm (Extended Data Fig. 5e) [67].
492 Upon activation Chm7 becomes associated with a unique site in the nuclear envelope (Figure 6a-
493 b). This active conformation can be induced by deleting auto-inhibitory helices in the ESCRT-III
494 domain [67] [herein $Chm7_{OPEN}$]. Strikingly, activated $Chm7_{OPEN}$ localized to a single site in the
495 nuclear envelope (Fig. 6a, panel *ii*; b) that co-localized with both INQ and JUNQ (Fig. 6a, panel
496 *ii*; b). These findings suggest this perinuclear ESCRT marks the site of INQ and JUNQ homing
497 and connects nuclear and cytoplasmic spatial PQC to vacuolar delivery. We next examined INQ
498 and JUNQ localization in *chm7Δ* cells. Both INQ and the JUNQ still formed and migrated to the
499 perinuclear region in *chm7Δ* cells, but they no longer converged to the same location (Fig. 6b).
500 These experiments indicate a novel role for the Chm7 ESCRT protein in recruiting nuclear and
501 cytoplasmic PQC compartments to the proper location on the nuclear envelope for further
502 clearance or terminal sequestration.

503 We also observe egress of the INQ from the nucleus into the cytoplasm when the nucleus becomes
504 untethered from the vacuole in *nvj1*Δ or *vac8*Δ mutants (Fig. 5f, g) or when vacuolar engulfment
505 is blocked in the *vps23Δ, vps34Δ, vps15Δ,* and *vps4*Δ mutants (Fig. 6c, f). Further, we do not see
506 the INQ enter the vacuole in *nvj1*Δ or *vps4*Δ mutants (Fig. 7h). Previous studies described a
507 perinuclear ESCRT-II/III protein Chm7 (CHMP7 in mammals), linked to remodeling nuclear
508 envelopes, clearance of misassembled nuclear pores, egress of herpes virus from the nucleus to the
509 cytosol, as well as nuclear envelope sealing and nuclear pore quality control [67]. We hypothesized
510 that Chm7 participates in the homing of the INQ and the JUNQ to aid in clearance via the vacuole.
511 This data is very intriguing and may provide a link between protein quality control and nuclear

envelope quality control. Future studies should determine whether additional forms of microautophagy, such as nucleophagy, ERphagy, piecemeal microautophagy of the nucleus, or selective autophagy of nuclear pore complexes participate in clearance of these PQC compartments.

Our analyses place spatial PQC in the larger context of cellular organization and inter-organellar communication [94] and uncover a role for nuclear pores and the nuclear envelope in communicating nucleocytoplasmic protein quality control decisions between the nucleus, the cytoplasm and the endolysosomal system. This idea is particularly intriguing given the link between nuclear pore dysfunction and aging, lamin progeria mutants and neurodegenerative diseases such as Huntington's disease, Amyotrophic Lateral Sclerosis and Frontal Temporal Dementia, which are all characterized by nuclear pore dysfunction and altered nucleocytoplasmic trafficking [31, 34, 35, 95-98]. Our findings raise the possibility that compromising nucleocytoplasmic trafficking leads to impaired misfolded protein clearance contributing to further cellular dysfunction. A better understanding of these pathways may provide fundamental insights into the critical biological process of protein quality control and point to avenues to ameliorate a large range of human disorders.

MAIN REFERENCES

1. Hartl, F.U., Bracher, A. & Hayer-Hartl, M. Molecular chaperones in protein folding and proteostasis. *Nature* **475**, 324-332 (2011).

532 2. Needham, P.G., Guerriero, C.J. & Brodsky, J.L. Chaperoning Endoplasmic Reticulum-
533 Associated Degradation (ERAD) and Protein Conformational Diseases. *Cold Spring*
534 *Harb Perspect Biol* **11** (2019).
535 3. Balchin, D., Hayer-Hartl, M. & Hartl, F.U. In vivo aspects of protein folding and quality
536 control. *Science* **353**, aac4354 (2016).
537 4. Sontag, E.M., Samant, R.S. & Frydman, J. Mechanisms and Functions of Spatial Protein
538 Quality Control. *Annu Rev Biochem* (2017).
539 5. Pohl, C. & Dikic, I. Cellular quality control by the ubiquitin-proteasome system and
540 autophagy. *Science* **366**, 818-822 (2019).
541 6. Finley, D. & Prado, M.A. The Proteasome and Its Network: Engineering for Adaptability.
542 *Cold Spring Harb Perspect Biol* **12** (2020).
543 7. Alberti, S. & Hyman, A.A. Are aberrant phase transitions a driver of cellular aging?
544 *Bioessays* (2016).
545 8. Ano Bom, A.P. *et al.* Mutant p53 aggregates into prion-like amyloid oligomers and
546 fibrils: implications for cancer. *J Biol Chem* **287**, 28152-28162 (2012).
547 9. Douglas, P.M. & Dillin, A. Protein homeostasis and aging in neurodegeneration. *J Cell*
548 *Biol* **190**, 719-729 (2010).
549 10. De Mattos, E.P. *et al.* Protein Quality Control Pathways at the Crossroad of
550 Synucleinopathies. *J Parkinsons Dis* **10**, 369-382 (2020).
551 11. Kaganovich, D., Kopito, R. & Frydman, J. Misfolded proteins partition between two
552 distinct quality control compartments. *Nature* **454**, 1088-1095 (2008).
553 12. Dillin, A. & Cohen, E. Ageing and protein aggregation-mediated disorders: from
554 invertebrates to mammals. *Philos Trans R Soc Lond B Biol Sci* **366**, 94-98 (2011).

555 13. Balch, W.E., Morimoto, R.I., Dillin, A. & Kelly, J.W. Adapting proteostasis for disease
556 intervention. *Science* **319**, 916-919 (2008).
557 14. Reichmann, D., Voth, W. & Jakob, U. Maintaining a Healthy Proteome during Oxidative
558 Stress. *Mol Cell* **69**, 203-213 (2018).
559 15. Morales-Polanco, F., Lee, J.H., Barbosa, N.M. & Frydman, J. Cotranslational
560 Mechanisms of Protein Biogenesis and Complex Assembly in Eukaryotes. *Annu Rev*
561 *Biomed Data Sci* **5**, 67-94 (2022).
562 16. Specht, S., Miller, S.B., Mogk, A. & Bukau, B. Hsp42 is required for sequestration of
563 protein aggregates into deposition sites in Saccharomyces cerevisiae. *J Cell Biol* **195**,
564 617-629 (2011).
565 17. Escusa-Toret, S., Vonk, W.I. & Frydman, J. Spatial sequestration of misfolded proteins
566 by a dynamic chaperone pathway enhances cellular fitness during stress. *Nat Cell Biol*
567 (2013).
568 18. Miller, S.B. *et al.* Compartment-specific aggregases direct distinct nuclear and
569 cytoplasmic aggregate deposition. *EMBO J* **34**, 778-797 (2015).
570 19. Weisberg, S.J. *et al.* Compartmentalization of superoxide dismutase 1 (SOD1G93A)
571 aggregates determines their toxicity. *Proc Natl Acad Sci U S A* **109**, 15811-15816 (2012).
572 20. Babazadeh, R. *et al.* Syntaxin 5 Is Required for the Formation and Clearance of Protein
573 Inclusions during Proteostatic Stress. *Cell Rep* **28**, 2096-2110 e2098 (2019).
574 21. Nollen, E.A. *et al.* Dynamic changes in the localization of thermally unfolded nuclear
575 proteins associated with chaperone-dependent protection. *Proc Natl Acad Sci U S A* **98**,
576 12038-12043 (2001).

577 22. Yasuda, S. *et al.* Stress- and ubiquitylation-dependent phase separation of the
578 proteasome. *Nature* **578**, 296-300 (2020).
579 23. Polling, S. *et al.* Misfolded polyglutamine, polyalanine, and superoxide dismutase 1
580 aggregate via distinct pathways in the cell. *J Biol Chem* **289**, 6669-6680 (2014).
581 24. Park, J.H. *et al.* Amyotrophic lateral sclerosis-related mutant superoxide dismutase 1
582 aggregates inhibit 14-3-3-mediated cell survival by sequestration into the JUNQ
583 compartment. *Hum Mol Genet* **26**, 3615-3629 (2017).
584 25. McClellan, A.J., Scott, M.D. & Frydman, J. Folding and quality control of the VHL
585 tumor suppressor proceed through distinct chaperone pathways. *Cell* **121**, 739-748
586 (2005).
587 26. Gupta, R. *et al.* Firefly luciferase mutants as sensors of proteome stress. *Nat Methods* **8**,
588 879-884 (2011).
589 27. Samant, R.S., Livingston, C.M., Sontag, E.M. & Frydman, J. Distinct proteostasis circuits
590 cooperate in nuclear and cytoplasmic protein quality control. *Nature* **563**, 407-411
591 (2018).
592 28. Popken, P., Ghavami, A., Onck, P.R., Poolman, B. & Veenhoff, L.M. Size-dependent
593 leak of soluble and membrane proteins through the yeast nuclear pore complex. *Mol Biol*
594 *Cell* **26**, 1386-1394 (2015).
595 29. Amm, I. & Wolf, D.H. Molecular mass as a determinant for nuclear San1-dependent
596 targeting of misfolded cytosolic proteins to proteasomal degradation. *FEBS Lett* **590**,
597 1765-1775 (2016).
598 30. Timney, B.L. *et al.* Simple rules for passive diffusion through the nuclear pore complex.
599 *J Cell Biol* **215**, 57-76 (2016).

600 31. Woerner, A.C. *et al.* Cytoplasmic protein aggregates interfere with nucleocytoplasmic
601 transport of protein and RNA. *Science* **351**, 173-176 (2016).
602 32. Park, S.H. *et al.* PolyQ Proteins Interfere with Nuclear Degradation of Cytosolic Proteins
603 by Sequestering the Sis1p Chaperone. *Cell* **154**, 134-145 (2013).
604 33. Neuber, A. *et al.* Nuclear export receptor Xpo1/Crm1 is physically and functionally
605 linked to the spindle pole body in budding yeast. *Mol Cell Biol* **28**, 5348-5358 (2008).
606 34. Grima, J.C. *et al.* Mutant Huntingtin Disrupts the Nuclear Pore Complex. *Neuron* **94**, 93-
607 107 e106 (2017).
608 35. Gasset-Rosa, F. *et al.* Polyglutamine-Expanded Huntingtin Exacerbates Age-Related
609 Disruption of Nuclear Integrity and Nucleocytoplasmic Transport. *Neuron* **94**, 48-57 e44
610 (2017).
611 36. Wente, S.R. & Blobel, G. A temperature-sensitive NUP116 null mutant forms a nuclear
612 envelope seal over the yeast nuclear pore complex thereby blocking nucleocytoplasmic
613 traffic. *J Cell Biol* **123**, 275-284 (1993).
614 37. Chen, L. *et al.* Sts1 plays a key role in targeting proteasomes to the nucleus. *J Biol Chem*
615 **286**, 3104-3118 (2011).
616 38. Takeda, K. & Yanagida, M. Regulation of nuclear proteasome by Rhp6/Ubc2 through
617 ubiquitination and destruction of the sensor and anchor Cut8. *Cell* **122**, 393-405 (2005).
618 39. Tatebe, H. & Yanagida, M. Cut8, essential for anaphase, controls localization of 26S
619 proteasome, facilitating destruction of cyclin and Cut2. *Curr Biol* **10**, 1329-1338 (2000).
620 40. Romero-Perez, L., Chen, L., Lambertson, D. & Madura, K. Sts1 can overcome the loss of
621 Rad23 and Rpn10 and represents a novel regulator of the ubiquitin/proteasome pathway.
622 *J Biol Chem* **282**, 35574-35582 (2007).

623 41. Aitchison, J.D., Blobel, G. & Rout, M.P. Nup120p: a yeast nucleoporin required for NPC
624 distribution and mRNA transport. *J Cell Biol* **131**, 1659-1675 (1995).
625 42. Heath, C.V. *et al.* Nuclear pore complex clustering and nuclear accumulation of poly(A)+
626 RNA associated with mutation of the Saccharomyces cerevisiae RAT2/NUP120 gene. *J*
627 *Cell Biol* **131**, 1677-1697 (1995).
628 43. Ader, C. *et al.* Amyloid-like interactions within nucleoporin FG hydrogels. *Proc Natl*
629 *Acad Sci U S A* **107**, 6281-6285 (2010).
630 44. Strawn, L.A., Shen, T., Shulga, N., Goldfarb, D.S. & Wente, S.R. Minimal nuclear pore
631 complexes define FG repeat domains essential for transport. *Nat Cell Biol* **6**, 197-206
632 (2004).
633 45. Parkinson, D.Y. *et al.* Nanoimaging cells using soft X-ray tomography. *Methods Mol*
634 *Biol* **950**, 457-481 (2013).
635 46. Le Gros, M.A. *et al.* Biological soft X-ray tomography on beamline 2.1 at the Advanced
636 Light Source. *J Synchrotron Radiat* **21**, 1370-1377 (2014).
637 47. Larabell, C.A. & Nugent, K.A. Imaging cellular architecture with X-rays. *Curr Opin*
638 *Struct Biol* **20**, 623-631 (2010).
639 48. Le Gros, M.A., McDermott, G., Uchida, M., Knoechel, C.G. & Larabell, C.A. High-
640 aperture cryogenic light microscopy. *J Microsc* **235**, 1-8 (2009).
641 49. Ekman, A. *et al.* Putting Molecules in the Picture: Using Correlated Light Microscopy
642 and Soft X-Ray Tomography to Study Cells, in *Synchrotron Light Sources and Free-*
643 *Electron Lasers: Accelerator Physics, Instrumentation and Science Applications*. (eds. E.
644 Jaeschke, S. Khan, J.R. Schneider & J.B. Hastings) 1-32 (Springer International
645 Publishing, Cham; 2019).

646 50. Ekman, A.A. *et al.* Mesoscale imaging with cryo-light and X-rays: Larger than molecular
647 machines, smaller than a cell. *Biol Cell* **109**, 24-38 (2017).
648 51. Huh, W.K. *et al.* Global analysis of protein localization in budding yeast. *Nature* **425**,
649 686-691 (2003).
650 52. Wu, G.H. *et al.* Multi-scale 3D Cryo-Correlative Microscopy for Vitrified Cells.
651 *Structure* **28**, 1231-1237.e1233 (2020).
652 53. Schuler, M.H. *et al.* Miro1-mediated mitochondrial positioning shapes intracellular
653 energy gradients required for cell migration. *Mol Biol Cell* **28**, 2159-2169 (2017).
654 54. Frottin, F. *et al.* The nucleolus functions as a phase-separated protein quality control
655 compartment. *Science* **365**, 342-347 (2019).
656 55. Velazquez, J.M. & Lindquist, S. hsp70: nuclear concentration during environmental
657 stress and cytoplasmic storage during recovery. *Cell* **36**, 655-662 (1984).
658 56. Falahati, H., Pelham-Webb, B., Blythe, S. & Wieschaus, E. Nucleation by rRNA Dictates
659 the Precision of Nucleolus Assembly. *Curr Biol* **26**, 277-285 (2016).
660 57. Azkanaz, M. *et al.* Protein quality control in the nucleolus safeguards recovery of
661 epigenetic regulators after heat shock. *Elife* **8** (2019).
662 58. Pan, X. *et al.* Nucleus-vacuole junctions in Saccharomyces cerevisiae are formed through
663 the direct interaction of Vac8p with Nvj1p. *Mol Biol Cell* **11**, 2445-2457 (2000).
664 59. Kohlwein, S.D. *et al.* Tsc13p is required for fatty acid elongation and localizes to a novel
665 structure at the nuclear-vacuolar interface in Saccharomyces cerevisiae. *Mol Cell Biol* **21**,
666 109-125 (2001).

667 60. Levine, T.P. & Munro, S. Dual targeting of Osh1p, a yeast homologue of oxysterol-
668 binding protein, to both the Golgi and the nucleus-vacuole junction. *Mol Biol Cell* **12**,
669 1633-1644 (2001).
670 61. Kvam, E. & Goldfarb, D.S. Structure and function of nucleus-vacuole junctions: outer-
671 nuclear-membrane targeting of Nvj1p and a role in tryptophan uptake. *J Cell Sci* **119**,
672 3622-3633 (2006).
673 62. Kvam, E. & Goldfarb, D.S. Nucleus-vacuole junctions and piecemeal microautophagy of
674 the nucleus in S. cerevisiae. *Autophagy* **3**, 85-92 (2007).
675 63. Roberts, P. *et al.* Piecemeal microautophagy of nucleus in Saccharomyces cerevisiae.
676 *Mol Biol Cell* **14**, 129-141 (2003).
677 64. Krick, R. *et al.* Piecemeal microautophagy of the nucleus requires the core
678 macroautophagy genes. *Mol Biol Cell* **19**, 4492-4505 (2008).
679 65. von Appen, A. *et al.* LEM2 phase separation promotes ESCRT-mediated nuclear
680 envelope reformation. *Nature* **582**, 115-118 (2020).
681 66. Thaller, D.J. & Patrick Lusk, C. Fantastic nuclear envelope herniations and where to find
682 them. *Biochem Soc Trans* **46**, 877-889 (2018).
683 67. Webster, B.M. *et al.* Chm7 and Heh1 collaborate to link nuclear pore complex quality
684 control with nuclear envelope sealing. *EMBO J* **35**, 2447-2467 (2016).
685 68. Thaller, D.J. *et al.* An ESCRT-LEM protein surveillance system is poised to directly
686 monitor the nuclear envelope and nuclear transport system. *Elife* **8** (2019).
687 69. Babst, M., Odorizzi, G., Estepa, E.J. & Emr, S.D. Mammalian tumor susceptibility gene
688 101 (TSG101) and the yeast homologue, Vps23p, both function in late endosomal
689 trafficking. *Traffic* **1**, 248-258 (2000).

690 70. Katzmann, D.J., Babst, M. & Emr, S.D. Ubiquitin-dependent sorting into the
691 multivesicular body pathway requires the function of a conserved endosomal protein
692 sorting complex, ESCRT-I. *Cell* **106**, 145-155 (2001).
693 71. Herrador, A., Léon, S., Haguenauer-Tsapis, R. & Vincent, O. A mechanism for protein
694 monoubiquitination dependent on a trans-acting ubiquitin-binding domain. *J Biol Chem*
695 **288**, 16206-16211 (2013).
696 72. Stack, J.H., Herman, P.K., Schu, P.V. & Emr, S.D. A membrane-associated complex
697 containing the Vps15 protein kinase and the Vps34 PI 3-kinase is essential for protein
698 sorting to the yeast lysosome-like vacuole. *EMBO J* **12**, 2195-2204 (1993).
699 73. Herman, P.K. & Emr, S.D. Characterization of VPS34, a gene required for vacuolar
700 protein sorting and vacuole segregation in Saccharomyces cerevisiae. *Mol Cell Biol* **10**,
701 6742-6754 (1990).
702 74. Burda, P., Padilla, S.M., Sarkar, S. & Emr, S.D. Retromer function in endosome-to-Golgi
703 retrograde transport is regulated by the yeast Vps34 PtdIns 3-kinase. *J Cell Sci* **115**,
704 3889-3900 (2002).
705 75. Slessareva, J.E., Routt, S.M., Temple, B., Bankaitis, V.A. & Dohlman, H.G. Activation
706 of the phosphatidylinositol 3-kinase Vps34 by a G protein alpha subunit at the endosome.
707 *Cell* **126**, 191-203 (2006).
708 76. Henne, W.M., Stenmark, H. & Emr, S.D. Molecular mechanisms of the membrane
709 sculpting ESCRT pathway. *Cold Spring Harb Perspect Biol* **5** (2013).
710 77. Hurley, J.H. & Hanson, P.I. Membrane budding and scission by the ESCRT machinery:
711 it's all in the neck. *Nat Rev Mol Cell Biol* **11**, 556-566 (2010).

712 78. Katayama, H., Kogure, T., Mizushima, N., Yoshimori, T. & Miyawaki, A. A sensitive
713 and quantitative technique for detecting autophagic events based on lysosomal delivery.
714 *Chem Biol* **18**, 1042-1052 (2011).
715 79. Bialecka-Fornal, M., Makushok, T. & Rafelski, S.M. A Review of Fluorescent Proteins
716 for Use in Yeast. *Methods Mol Biol* **1369**, 309-346 (2016).
717 80. Sitron, C.S., Park, J.H., Giafaglione, J.M. & Brandman, O. Aggregation of CAT tails
718 blocks their degradation and causes proteotoxicity in S. cerevisiae. *PLoS One* **15**,
719 e0227841 (2020).
720 81. Schuck, S., Gallagher, C.M. & Walter, P. ER-phagy mediates selective degradation of
721 endoplasmic reticulum independently of the core autophagy machinery. *J Cell Sci* **127**,
722 4078-4088 (2014).
723 82. Haupts, U., Maiti, S., Schwille, P. & Webb, W.W. Dynamics of fluorescence fluctuations
724 in green fluorescent protein observed by fluorescence correlation spectroscopy. *Proc Natl*
725 *Acad Sci U S A* **95**, 13573-13578 (1998).
726 83. Shinoda, H., Shannon, M. & Nagai, T. Fluorescent Proteins for Investigating Biological
727 Events in Acidic Environments. *Int J Mol Sci* **19** (2018).
728 84. Klionsky, D.J. *et al.* Guidelines for the use and interpretation of assays for monitoring
729 autophagy (4th edition). *Autophagy* **17**, 1-382 (2021).
730 85. Eising, S. *et al.* A lysosomal biogenesis map reveals the cargo spectrum of yeast vacuolar
731 protein targeting pathways. *J Cell Biol* **221** (2022).
732 86. Waite, K.A., De-La Mota-Peynado, A., Vontz, G. & Roelofs, J. Starvation Induces
733 Proteasome Autophagy with Different Pathways for Core and Regulatory Particles. *J Biol*
734 *Chem* **291**, 3239-3253 (2016).

735 87. Kvam, E. & Goldfarb, D.S. Nvj1p is the outer-nuclear-membrane receptor for oxysterol-
736 binding protein homolog Osh1p in Saccharomyces cerevisiae. *J Cell Sci* **117**, 4959-4968
737 (2004).
738 88. Vida, T.A. & Emr, S.D. A new vital stain for visualizing vacuolar membrane dynamics
739 and endocytosis in yeast. *J Cell Biol* **128**, 779-792 (1995).
740 89. Thorn, K. Genetically encoded fluorescent tags. *Mol Biol Cell* **28**, 848-857 (2017).
741 90. Costantini, L.M. *et al.* A palette of fluorescent proteins optimized for diverse cellular
742 environments. *Nat Commun* **6**, 7670 (2015).
743 91. Amm, I., Sommer, T. & Wolf, D.H. Protein quality control and elimination of protein
744 waste: the role of the ubiquitin-proteasome system. *Biochim Biophys Acta* **1843**, 182-196
745 (2014).
746 92. Eisele, F. *et al.* An Hsp90 co-chaperone links protein folding and degradation and is part
747 of a conserved protein quality control. *Cell Rep* **35**, 109328 (2021).
748 93. Kumar, B. *et al.* ESCRT-I Protein Tsg101 Plays a Role in the Post-macropinocytic
749 Trafficking and Infection of Endothelial Cells by Kaposi's Sarcoma-Associated
750 Herpesvirus. *PLoS Pathog* **12**, e1005960 (2016).
751 94. Gottschling, D.E. & Nystrom, T. The Upsides and Downsides of Organelle
752 Interconnectivity. *Cell* **169**, 24-34 (2017).
753 95. Zhang, K. *et al.* The C9orf72 repeat expansion disrupts nucleocytoplasmic transport.
754 *Nature* **525**, 56-61 (2015).
755 96. Fallini, C., Khalil, B., Smith, C.L. & Rossoll, W. Traffic jam at the nuclear pore: All
756 roads lead to nucleocytoplasmic transport defects in ALS/FTD. *Neurobiol Dis* **140**,
757 104835 (2020).

758 97. Shang, J. *et al.* Aberrant distributions of nuclear pore complex proteins in ALS mice and
759 ALS patients. *Neuroscience* **350**, 158-168 (2017).
760 98. Chou, C.C. *et al.* TDP-43 pathology disrupts nuclear pore complexes and
761 nucleocytoplasmic transport in ALS/FTD. *Nat Neurosci* **21**, 228-239 (2018).

762

763 **FIGURE TITLES AND LEGENDS**

764 **Figure 1: The INQ and JUNQ are separate nuclear and cytoplasmic PQC compartments.**
765 (a) Schematic showing nuclear and cytoplasmic misfolded proteins could be sequestered into
766 separate compartments or the cytoplasmic misfolded proteins could be imported into the nucleus
767 and sequestered into the nuclear PQC compartment INQ. (b) Experimental schematic.
768 Temperature sensitive Luciferase is properly folded at 25 °C. Heat shock at 37 °C leads to
769 unfolding and sequestration of the protein. Degradation of the unfolded and sequestered proteins
770 can be blocked by treatment with the proteasome inhibitor MG132. (c, d) Live-cell time-lapse
771 fluorescence microscopy of WT cells expressing NLS-LuciTs (c) or NES-LuciTs (d) at 37 °C,
772 treated with DMSO (top) or 100μM MG132 (bottom). Representative still frames at the times
773 shown. Scale bars are 1μm. (e, f) Representative SIM images of WT cells expressing NLS-
774 LuciTs (e) or NLS-VHL (f) after 2 hr at 37 °C and treated with 100μM MG132. NLS-LuciTs
775 and NLS-VHL are shown in green, nuclear pores in gold, and Hoechst counterstain in blue. Scale
776 bars are 1μm. Line intensity profiles indicate relative locations of subcellular compartments to
777 Nups and DNA. (g, h) Representative SIM images of WT cells expressing NES-LuciTs (g) and
778 NES-VHL (h) after 2 hr at 37 °C and treated with 100μM MG132. NES-LuciTs and NES-VHL
779 are shown in purple, nuclear pores in gold, and Hoechst counterstain in blue. Scale bars are 1μm.
780 Line intensity profiles indicate relative locations of subcellular compartments to Nups and DNA.

781 **Figure 2: Nuclear entry of misfolded proteins is not required for clearance. .**

782 (a) Representative SIM images of WT cells expressing Ubc9Ts-GFP after 2h at 37 °C treated
783 with DMSO (a) or 100μM MG132 (b). Ubc9Ts-GFP is shown in green, nuclear pores in gold,
784 and Hoechst counterstain in blue. Scale bars are 1μm. Line intensity profiles indicate relative
785 locations of subcellular compartments to Nups and DNA. (c) Representative confocal
786 fluorescence microscopy images of cells expressing sGFP with DMSO (control), 100μM MG132
787 treatment, co-expression of mHTT97QΔP or 200nM Leptomycin B treatment. Ratio of
788 cytoplasmic:nuclear fluorescence is shown in d. Kruskal-Wallis test with Dunn's multiple
789 comparisons test was performed using Prism. Adjusted p value of No Treatment vs. MG132 is
790 0.0014, No Treatment vs. 97QΔP is 0.0027 and No Treatment vs. LMB is <0.0001. A minimum
791 of 500 cells per condition from 3 biologically independent experiments were analyzed. All scale
792 bars are 1μm. (e) Schematic illustrating the clearance of Ubc9Ts in WT yeast. (*ii*) Timeline of
793 treatments for clearance measurements with shift to 37 °C 60 minutes before initiation of the
794 measurements. (f) Schematic illustrating the *nup116-5* yeast have sealed nuclear pores at 37 °C,
795 thus blocking nucleocytoplasmic trafficking. (*ii*) Densitometric quantification of Western blot
796 bands (*iii*) measuring the amount of Ubc9Ts-EGFP remaining in shut-off experiment of WT vs
797 *nup116*-5 cells relative to $t = 0$ (mean ± s.e.m. from three biologically independent experiments)
798 fitted with a one-phase decay non-linear fit regression line. (g) Schematic illustrating the *sts1-2*
799 yeast do not translocate proteasomes to the nucleus at 37 °C. (*ii*) Densitometric quantification of
800 Western blot bands (iii) measuring the amount of Ubc9Ts-EGFP remaining in shut-off
801 experiment of WT vs sts1-2 cells relative to t = 0 (mean ± s.e.m. from three biologically
802 independent experiments) fitted with a one-phase decay non-linear fit regression line.

803 **Figure 3: INQ and JUNQ home to similar location on each side of the nuclear envelope via**
804 **a cytoplasmic signal linked to nuclear pores.**
805 WT cells co-expressing NLS-GFP-LuciTs and NES-DsRed-LuciTs were shifted to 37 °C, treated
806 with 100μM MG132 and monitored by live cell time-lapse fluorescence. Representative still
807 frames at the times shown. Scale bar is 1μm. (b) Graph of the distance between the INQ and
808 JUNQ compartments by particle tracking of inclusions from cell shown in (a) over the time
809 course of the experiment. The slight variations of tethered distance between 60 and 90 minutes is
810 likely due to the relative migration of one of the inclusions around a cellular structure as this
811 fluctuation can be seen at different times post-tethering in other cells (not shown). (c)
812 Representative SIM image taken of cells co-expressing NLS-EGFP-LuciTs and NES-DsRed-
813 LuciTs after 2 hr at 37 °C and treated with 100μM MG132. NLS-fusion proteins are shown in
814 green, NES-fusion proteins in purple, nuclear pores in gold, and Hoechst counterstain in blue.
815 Scale bar is 1μm. Line intensity profiles indicate relative locations of subcellular compartments
816 and Nups. (d) Representative confocal microscopy images taken of WT and 3 separate *nup120Δ*
817 yeast cells expressing NES-LuciTs (*i*), NLS-LuciTs (*ii*) or co-expressing NLS- and NES-LuciTs
818 (*iii*) after 2 hr at 37 °C. NLS-LuciTs is shown in green, NES-LuciTs in purple, nuclear pores in
819 gold, and Hoechst counterstain in blue. Scale bar is 1μm. Schematics on the right summarize the
820 findings of the data. (e) Schematic summarizing the data that the JUNQ localizes to the nuclear
821 pores. A signal is transmitted through or near the nuclear pores to recruit the INQ to the same
822 location, resulting in the homing of the 2 compartments.

823 **Figure 4: INQ resides near the nucleolus, JUNQ is surrounded by mitochondria, and both**
824 **compartments home into the Nuclear-Vacuolar Junction.**
825 (a) Unfixed, intact yeast cells are frozen in a capillary tube and imaged by fluorescence
826 microscopy and then X-ray tomography. The linear absorption coefficients are measured from
827 the tomography data and used to identify the subcellular compartments and organelles. The
828 fluorescence images are then correlated to the X-ray tomography data and 3D reconstructions of
829 the subcellular components are generated to determine the cellular context of the PQC
830 compartments. (b) WT cells co-expressing Hsp104-GFP from the endogenous locus and
831 HTT97QP-ChFP after 30 mins at 37 °C. (left) X-ray tomograms without and with fluorescence
832 overlay to indicate sites of Hsp104-GFP positive inclusions and HTT97QP-ChFP inclusion.
833 (right) Table of Linear Absorption Coefficient (LAC) values from the X-ray tomograms used to
834 annotate the images and generate a 3D reconstruction shown in panel c. (c) 3D reconstruction of
835 fluorescence correlated X-ray tomograms showing the JUNQ residing 450nm outside the barrier
836 of the nucleus as defined by the location of the nuclear envelope in the X-ray data (inset, top)
837 and the IPOD marked by mHTT (inset, bottom). JUNQ is shown in green, IPOD in orange,
838 nucleus in yellow, mitochondria in cyan, vacuoles in gray, and lipid droplets in white. Scale bar
839 on X-ray 3D reconstruction is 1μm, insets are 0.5μm. (d) 3D reconstruction of X-ray tomograms
840 from cell expressing NES-LuciTs after 90 mins heat shock at 37 °C and treated with 100μM
841 MG132. The Q-bodies can be seen to coalesce into the JUNQ compartment just outside the
842 nuclear boundary (inset ii). The Q-bodies also interact with vacuoles and the site of coalescence
843 into the JUNQ compartment is surrounded by a mitochondrial cage (inset i). Q-bodies and IPOD
844 are shown in purple, nucleus in yellow, mitochondria in cyan, vacuoles in gray, and lipid
845 droplets in white. Scale bar on X-ray 3D reconstruction is 1μm, insets are 0.5μm. (e) Q-bodies

846 can be seen interacting with mitochondria in a separate cell expressing NES-LuciTs. Q-bodies
847 are shown in purple, nucleus in yellow, nucleolus in gold, mitochondria in cyan, and vacuoles in
848 gray. Scale bar on X-ray 3D reconstruction is 1μm, inset is 0.5μm. (f) Same 3D reconstruction of
849 X-ray tomograms from cell expressing NES-LuciTs after 90 mins heat shock at 37 °C as shown
850 in d. Insets are from the same cell rotated 180°. Blue arrows indicate sites where Q-bodies are
851 directly interacting with the vacuoles. Red arrows indicate sites of nuclear-vacuolar junctions.
852 Scale bar on X-ray 3D reconstruction is 1μm, insets are 0.5μm. (g) 3D reconstruction of X-ray
853 tomograms from cell expressing NLS-LuciTs after 90 mins heat shock at 37 °C and treated with
854 100μM MG132. The INQ resides 400nm from the nucleolus (inset). INQ is shown in green,
855 nucleus in yellow, nucleolus in gold, mitochondria in cyan, and vacuoles in gray. Scale bar on X-
856 ray 3D reconstruction is 1μm, inset is 0.5μm. (h) Schematic illustrating the novel findings of the
857 association between mitochondria and all 3 cytoplasmic PQC compartments, the proximity of the
858 INQ to the nucleolus, the interaction between Q-bodies and the vacuole, and the hypothesized
859 location of the INQ and JUNQ at the nuclear vacuolar junction. The inset highlights two of the
860 component proteins of the NVJ, Nvj1 and Vac8, that are required for Piecemeal Microautophagy
861 of the Nucleus.

862 **Figure 5: JUNQ and INQ converge at the Nuclear-Vacuolar Junction to facilitate**
863 **clearance.**
864 (a) Endogenously tagged Nvj1-GFP yeast expressing NES—DsRed-LuciTs were shifted to 37
865 °C and monitored by live cell time-lapse fluorescence microscopy for the times shown. White
866 arrowheads indicate locations of Nvj1 punctum while yellow arrowheads indicate NES-LuciTs
867 punctum. Scale bar is 1μm. Representative SIM images of WT yeast co-expressing NES-DsRed-
868 LuciTs (b) or NLS-DsRed-LuciTs (c) and Nvj1-sfGFP after 2 hr incubation at 37 °C with
869 100μM MG132. Panel *ii* of both (b) and (c) are insets to better visualize the relative location of
870 the JUNQ and INQ to the Nvj1. Panel *iii* of both (b) and (c) are additional cells to illustrate other
871 phenotypes seen in the experiment. NES-DsRed-LuciTs is shown in purple, NLS-DsRed-LuciTs
872 is shown in green, Nvj1-sfGFP is shown in yellow, and DNA is shown in blue. Scale bars are 1
873 μm. (d) Representative confocal image of WT yeast expressing Nvj1-sfGFP (shown in yellow)
874 stained with FM4-64 vacuolar dye (shown in cyan). Scale bar is 1μm. (e) Representative SIM
875 image of WT yeast cell co-expressing NLS-DsRed-LuciTs (shown in green) with Nvj1-sfGFP
876 (shown in yellow) after 2 hr incubation at 37 °C with 100μM MG132. The NLS-LuciTs can be
877 seen extruding through the NVJ toward the vacuole. Scale bar is 1μm. (f) WT (top) and *nvj1Δ*
878 (bottom) cells co-expressing NLS-LuciTs and NES-LuciTs were shifted to 37 °C, treated with
879 100μM MG132 and monitored by live cell time-lapse fluorescence microscopy for the times
880 shown. White arrowheads indicate inclusions of NLS-LuciTs pulled into the cytoplasm. Scale
881 bars are 1μm. (g) Representative confocal images of WT, *nvj1Δ*, and *vac8Δ* yeast co-expressing
882 NLS-EGFP-LuciTs and NES-DsRed-LuciTs after 2 hr at 37 °C and treated with 100μM MG132.
883 NLS-EGFP-LuciTs is shown in green, NES-DsRed-LuciTs in purple, nuclear pores in gold, and
884 Hoechst counterstain in blue. White arrows indicate cytoplasmic localization of NLS-LuciTs.

885 Scale bar is 1μm. (h) Quantitation of the percentage of cells containing inclusions in WT, *nvj1Δ*,
886 and *vac8Δ* yeast co-expressing NLS-EGFP-LuciTs (*i*) and NES-DsRed-LuciTs (*ii*) after 2 hr
887 incubation at 37 °C with 100μM MG132. A minimum of 500 cells per condition from 3
888 biologically independent experiments were counted and unpaired Student's t-tests were
889 performed comparing the deletion strains to WT. P values were adjusted using two-stage linear
890 step-up procedure of Benjamini, Krieger, and Yekutieli with a false discovery rate (Q) of 5%.
891 Adjusted P value for NLS-LuciTs: WT vs *nvj1Δ* is 0.0205, WT vs *vac8Δ* is 0.0406. Adjusted P
892 value for NES-LuciTs: WT vs *nvj1Δ* is 0.013, WT vs *vac8Δ* is 0.0008. (i) Drop tests showing
893 serial dilutions of WT, *nvj1Δ*, and *vac8Δ* yeast at 30 and 37 °C with no treatment and 0.5mg/mL
894 AZC treatment after 72 h growth at indicated temperature. *nvj1Δ* and *vac8Δ* yeast have a growth
895 defect when subjected to proteostatic stress by AZC treatment.

896 **Figure 6: ESCRT-mediated extrusion from the nucleus and clearance.**
897 (a) The ESCRT-II/-III protein Chm7 has been shown to play a role in clearance of defective
898 nuclear pores and nuclear membrane quality control, therefore, it may be involved in the homing
899 of INQ and JUNQ to the NVJ. (*ii*) Representative confocal images of WT yeast co-expressing
900 $Chm7_{OPEN}$-EGFP and either NLS-DsRed-LuciTs (top) or NES-DsRed-LuciTs (bottom) after 2 hr
901 at 37 °C and treated with 100μM MG132. $Chm7_{OPEN}$ is shown in teal, NLS-DsRed-LuciTs in
902 green, NES-DsRed-LuciTs in purple, nuclear pores in gold and Hoechst counterstain in blue.
903 Arrows indicate locations of puncta for each protein. Scale bar is 1μm. (b) Representative
904 confocal images of WT and *chm7Δ* yeast co-expressing NLS-EGFP-LuciTs and NES-DsRed-
905 LuciTs after 120 minutes at 37 °C and treated with 100μM MG132. NLS-EGFP-LuciTs is shown
906 in green, NES-DsRed-LuciTs in purple, nuclear pores in gold, and Hoechst counterstain in blue.

907 Arrows indicate locations of puncta for each protein. Scale bar is 1μm. (c) ESCRT-family
908 proteins Vps23, Vps34, and Vps15 may be involved in clearance of INQ and JUNQ.
909 Representative confocal images of WT and *vps23Δ* , *vps34Δ,* and *vps15Δ* yeast co-expressing
910 NLS-EGFP-LuciTs and NES-DsRed-LuciTs after 2 hr at 37 °C and treated with 100μM MG132.
911 NLS-EGFP-LuciTs is shown in green, NES-DsRed-LuciTs in purple, nuclear pores in gold, and
912 Hoechst counterstain in blue. Insets show the budding INQ encapsulated by nuclear pores. Scale
913 bars are 1μm. (d) ESCRTIII proteins and the ATPase Vps4 are known to remodel membranes
914 and could be involved in vacuolar import of PQC compartments. (e) Quantitation of the
915 percentage of cells containing inclusions of NLS- or NES-LuciTs in WT and *vps4Δ* yeast co-
916 expressing NLS-EGFP-LuciTs and NES-DsRed-LuciTs after 2 hr incubation at 37 °C with
917 100μM MG132. A minimum of 300 cells per condition from 2 biologically independent
918 experiments were counted and Student's T tests were performed comparing the deletion strains
919 to WT. P value for WT vs *vps4Δ* NLS-LuciTs is 0.0007, and WT vs *vps4Δ* NES-LuciTs is
920 0.0018. (f) Representative confocal images of WT and *vps4Δ* yeast co-expressing NLS-EGFP-
921 LuciTs and NES-DsRed-LuciTs after 2 hr at 37 °C and treated with 100μM MG132. NLS-
922 EGFP-LuciTs is shown in green, NES-DsRed-LuciTs in purple, nuclear pores in gold, and
923 Hoechst counterstain in blue. Green arrows indicate cytoplasmic localization of NLS-LuciTs.
924 Scale bar is 1μm.

925

926 **Figure 7: Vacuolar clearance of the INQ and JUNQ**

927 (a) Possible routes of entry into the vacuole for the INQ and JUNQ. (b) Schematic of the LuciTs-
928 Keima experiments. (c) WT cells expressing NLS-2xKeima-LuciTs after 2 hr incubation at 37
929 °C with 100μM MG132. Over time, fluorescence is seen with excitation in the 589nm channel
930 indicating the NLS-LuciTs has encountered an acidic environment. Inset shows the transition
931 from green to red and a structure leaving the inclusion that is fully red. Scale bars are 5 uM. (d)
932 Representative images of WT cells expressing NES-2xKeima-LuciTs after 2 hr incubation at 37
933 °C with 100μM MG132. Over time, fluorescence is seen with excitation in the 589nm channel
934 indicating the NLS-LuciTs has encountered an acidic environment. Insets show the transition
935 from green to red and a structure leaving the inclusion that is fully red. Scale bars are 5 uM.
936 Representative Western Blots of NLS-GFP-LuciTs (e) and NES-GFP-LuciTs (f) in WT and
937 *pep4Δ* yeast. *pep4Δ* yeast were also treated with 1mM PMSF to completely inhibit vacuolar
938 proteases. A decrease in fragments can be seen in both the NLS- (e) and NES- (f) blots. (g)
939 Densitometric quantification of Western blot bands measuring the amount of full-length LuciTs-
940 GFP remaining in shut-off experiment as well as the fragments generated during clearance. The
941 ratio of fragment intensity to full-length protein is shown in the graph (mean ± s.e.m. from three
942 biologically independent experiments). One-way ANOVA was performed using Prism software
943 followed by Dunnett's multiple comparisons test. Adjusted P value for WT vs *pep4Δ* NLS-
944 LuciTs is 0.0018, and WT vs pep*4Δ* NES-LuciTs is 0.0220. (h) WT, *nvj1Δ*, and *vps4Δ* yeast
945 expressing NLS-GFP-LuciTs were treated with 8uM of FM4-64 and incubated for 2hr at 37 °C
946 with 100μM MG132. Cells were imaged every 5 mins for 90 mins. Scale bar is 1μm.

947

948

949 **Figure 8: Principles of Nuclear and Cytoplasmic spatial protein quality control**Model for
950 vacuolar targeting and clearance of nuclear and cytoplasmic protein inclusions in yeast. (a) Upon
951 heat shock, cytoplasmic and nuclear LuciTs locally misfold, and recruit chaperones and other PQC
952 factors that facilitate the subcellular spatial sequestration on distinct protein quality control
953 inclusions: (b) the Intranuclear Quality Control compartment (INQ) in the nucleus and Q-bodies
954 in the cytoplasm.(c) Q-bodies then coalesce to form the Juxtanuclear Quality Control compartment
955 (JUNQ), and misfolded proteins located in the INQ and the JUNQ can be degraded by the UPS
956 system in the nucleus and the cytoplasm respectively c.ii). (d) Alternatively, under conditions of
957 limited proteasomal activity, INQ and JUNQ can converge on the periphery of the nuclear
958 envelope, a mechanism mediated by the nuclear pores (homing)(e) The homing mechanism could
959 represent a coordinated way to target both inclusions for clearance at the vacuole. (e.ii) Vacuolar
960 mediated clearance of both INQ and JUNQ. ESCRT-family proteins are involved in organizing
961 the INQ and JUNQ for vacuolar degradation.

962 **METHODS**

963 **Time resolved live cell imaging.** Cells were grown overnight in raffinose media followed by 4–
964 6 h at 28 °C in galactose media to induce the expression. Cells were then immobilized on
965 concanavalin A-coated coverslips. Samples were washed in glucose media and kept in the same
966 medium by sealing the coverslips to slides with vacuum grease. When indicated, cells were treated
967 10 min before sealing with 100 uMof MG132 (Sigma) before sealing. Images were taken every 15
968 s for 60 min at 37 °C (or room temperature (25 °C)) using a Zeiss Axio Observer.Z1 inverted
969 microscope equipped with X-cite 120 LED light source (Lumen Dynamics), HE GFP/Cy3/DAPI
970 shift free filter sets (Zeiss), a Plan-Apochromat 100x/1.4 oil DIC M27 objective (Zeiss) and a
971 digital Axiocam MRm camera (Zeiss) controlled with the Zen blue software.

972 **Cycloheximide chase of preformed inclusions.** Cells were grown overnight in raffinose media,
973 back diluted to an OD600 of 0.1 in a 10 ml of galactose media and grown at 25 °C for 5 hours to
974 induce expression of both NLS and NES constructs. Cells were then resuspended in 10 ml of
975 glucose media at 100 uM MG132 and incubated for additional 15 min 25 °C and then switched to
976 37 °C for 30 minutes to ensure inclusion formation before CHX chase. Cells were then
977 immobilized on concanavalin deltaT culture dish (Fischer Scientific), washed with prewarmed
978 glucose media and incubated with glucose media supplemented with 100 uM MG132 and 50mg/ml
979 of cycloheximide (CHX)._Images were taken every 25 s for 120 min at 37 °C as mentioned above.

980 **FM4-64 vacuole labeling.** 10 ml of cells were grown on galactose media to a final OD600 of 0.8
981 at 25°C. Vacuolar dye was added by resuspending the cells on 2 ml of fresh galactose media plus
982 FM4-64 to a final concentration of 8uM, and incubated 30 min at 25°C. For imaging, cells were
983 then resuspended in glucose media at 100uM MG132 and incubated 20 min at 37°C to induce
984 inclusion formation. Cells were adhered on a concanavalin deltaT culture dish and imaged as
985 mentioned above.

986 **Immunostaining.** As in the live-cell imaging assay, cells were grown overnight in raffinose media
987 followed by 4–6 h at 28 °C in galactose media to induce the expression. Then, the cells were heat-
988 shocked at 37 °C in glucose media for 1 h before fixation in 4% paraformaldehyde for 15 mins at
989 37 °C followed by methanol fixation for 20 mins at -20 °C. Immunostaining proceeded as in [1].
990 Briefly, samples were resuspended in sorbitol buffer and spheroplasted in Zymolyase (Zymo) for
991 30 mins at room temperature and further solubilized in 0.1% Triton X-100 for 10 mins. Antibodies
992 are diluted in Buffer WT (1% nonfat dry milk 0.5 mg/ml BSA 200 mM NaCl 50 mM HEPES–
993 KOH (pH 7.5) 1 mM NaN3 0.1% Tween-20) at a 1:500 dilution and incubated 2 hr at room
994 temperature or overnight at 4 °C. Samples are then washed in Buffer WT followed by incubation

995 in secondary antibodies at a 1:1000 dilution for 2 hr at room temperature. Cells were immobilized
996 on poly-lysine coated coverslips and mounted in Prolong Diamond mounting media (with DAPI
997 where indicated) (Thermo-Fisher). Nanobodies against GFP and RFP were conjugated to Alexa
998 Fluor 488 and Alexa Fluor 568 respectively and used to amplify the signal from the fluorescent
999 proteins during the SIM measurements. Anti-Nsp1 antibody from EnCor Biotechnology was used
1000 to visualize nuclear pores and Anti-Nsr1 antibody from Abcam was used for staining the nucleolus.

1001 **Confocal microscopy.** Confocal microscopy on immunostained samples was performed on a
1002 Zeiss LSM 700 inverted confocal microscope with 405, 488, 555 and 639 nm laser lines with Basic
1003 Filterset for LSM700 (Zeiss), a Plan-Apochromat 100x/1.4 oil DIC WD=0.17 objective (Zeiss)
1004 and a digital Axiocam MRm camera (Zeiss) controlled with the Zen black software. Confocal data
1005 sets were deconvolved when indicated using the Zen software with a fast-iterative function.
1006 Fluorescence was quantified where indicated using ImageJ software (NIH). The sGFP intensity
1007 measurements, were performed as described previously [2]. Briefly, the raw integrated density
1008 (herein indicated as intensity) was measured for the nucleus and the whole cell. The intensity value
1009 of the nucleus was then divided by the area. The cytoplasmic intensity was calculated by
1010 subtracting the nuclear intensity from the whole cell intensity and the cytoplasmic area by
1011 subtracting the nuclear area from the whole cell area. The cytoplasmic intensity was then divided
1012 by the cytoplasmic area. Finally, the ratio of cytoplasmic to nuclear was calculated by dividing the
1013 cytoplasmic intensity per area by the nuclear intensity per area. Statistical analysis was performed
1014 using Prism (GraphPad).

1015 **Super-resolution microscopy**. Structured illumination microscopy (SIM) on immunostained
1016 samples was performed using an OMX V4 Blaze system (Applied Precision, GE Healthcare)
1017 equipped with a 100×/1.40 NA PlanApo oil-immersion objective (Olympus), 405, 488, 568 and

1018 647 nm diode lasers with standard filter sets, and 3 emCCD cameras (Photometrics Evolve 512).
1019 SIM data were acquired with a Z-distance of 125 nm and with 15 images per plane (five phases,
1020 three angles). The raw data was computationally reconstructed using a Wiener (high-frequency)
1021 filter setting of between 0.001 and 0.003 and channel- specific OTFs employing the softWoRx
1022 version 6.5.2 software package (GE Healthcare) to obtain a super-resolution image stack. 3D
1023 reconstructions and line intensity profiles were generated in Volocity version 6.3 (Perkin Elmer).

1024 To construct *NVJ1-sfGFP* strain with integrated sfGFP fusion at the C-terminal, sf*GFP* was
1025 knocked-in via standard PCR-based homologous recombination. The *sfGFP* cassette was
1026 amplified from plasmid GTL-g (Addgene plasmid #81099) with oligonucleotides

1027 5'TAGATGCACAAGTGAACACTGAACAAGCATACTCTCAACCATTTAGATACGCGGC
1028 CGCTCTAGAACTA and

1029 5' TCGCACCTCGTTGTAAGTGACGATGATAACCGAGATGACGGAAATATAGTACA

1030 ATGGAAAAACGCCAGCAACG. The cassette was amplified, separated by electrophoresis, gel
1031 purified and transformed into yeast cells using the lithium acetate method. Correct transformants
1032 were verified by standard PCR using the oligonucleotides NVJ1-VF:
1033 5'GGATACCAGAACAACCTCTTC, NVJ1-VR: 5' ATGCCCGGCGTTATATATTGC, and
1034 LEU2-VF: 5' AGCACGAGCCTCCTTTACCT.

1035 **Keima cloning.** The NLS-Keima-luciTS plasmid was constructed by replacing the GFP moeity
1036 with yeast optimized Keima using a cassette amplified from plasmid pFA6a-link-yomKeima-
1037 Kan (Addgene plasmid #44902) with the oligonucleotides

1038 5'ATGGCTTCTCCTAAGAAGAAACGTAAAGTTATGGTTTCTGTGATCGCTAAACAAAT
1039 GAC and

1040 5'CCATGCAAGCTTGCGCGGATCCGCGCCCTAATAGAGAATGTCTTGCGATAGC.

1041 Similarly, the NES-Keima-luciTS plasmid was created replacing the GFP moity using the
1042 olinucleotides

1043 5'CTCGCACTTAAGTTCGCCGGTTTAGACCTGATGGTTTCTGTGATCGCTAAACAAAT
1044 GAC and
1045 5'CCATGCAAGCTTGCGCGGATCCGCGCCCTAATAGAGAATGTCTTGCGATAGC. To
1046 construct the NLS and NES-2xKeima-luciTS, an additional Keima moeity was created by
1047 inserting a second keima cassette amplified using the oligonucleotides
1048 5'CCATGCAAGCTTGCGCGGATCCGCGCCCTAATAGAGAATGTCTTGCGATAGC and
1049 5'TTCCATGCAAGCTTGCGCGGATCCGCGCCCTAATAGAGAATGTCTTGCGA.

1050 **Live cell LeicaSp8/sSTED microscopy of Keima-tagged inclusions.** Cells were grown as for
1051 time resolve live fluorescent microscopy, adhered on concanavalin deltaT culture dish and
1052 examined at 37 °C for 90 minutes. Representative cells were collected every 5 minutes on a
1053 Leica TCS SP8 inverted sSTED microscope equipped with a 100x/1.40 APO objective and using
1054 the following detection mirror settings: Keima 590-650nm. Cells were sequentially excited using
1055 404nm and 568 nm laser. One representative middle slide was acquired, and images were
1056 deconvolved and background subtracted using Huygens Professional (Scientific Volume
1057 Imaging).

1058 **Xray-tomography**:

1059 **Preparation of Specimen Mounting Capillaries.**Thin-walled glass capillaries were pulled as
1060 described in [3]. After being cut to length, capillaries were dipped in poly-L-lysine (0.01% solution,
1061 Tissue Culture Grade, Sigma Aldrich, St. Louis, MO). Fiducial markers, used to align soft x-ray
1062 projection images to a common axis, were generated by briefly immersing the capillaries a solution
1063 of 100 nm gold nanoparticles (EMGC100, BBI International, Cardiff, CF14 5DX, UK), rinsing
1064 and then drying them in air.

1065 Specimen capillaries for use in correlated imaging experiments were prepared as above and then
1066 dipped in a suspension of red polystyrene microspheres (FluoSpheres Carboxylate-Modified
1067 Microspheres, 0.2 µm, Dark Red Fluorescent (660 excitation/ 680 emission), Life Technologies,
1068 Invitrogen). The polystyrene microspheres were used fiducial markers for the alignment of
1069 fluorescence images to each other and for the co-alignment of soft x-ray and cryo- fluorescence
1070 tomographic reconstructions.

1071 **Specimen Mounting.**1 ml of yeast cells in mid-log phase growth (OD_{600} ~0.5) were pelleted and
1072 re-suspended in ~50µl media. 1µl of this suspension was transferred into a specimen capillary
1073 using a standard micropipette. The capillary contents were immediately cryopreserved by rapid
1074 plunging into liquid propane at 165°C using a custom apparatus. Cryopreserved specimens were
1075 transferred into storage boxes using a home-built cryo-transfer device and stored in a Dewar held
1076 at 77K [3].

1077 **Imaging Cells in the Cryogenic Confocal Light Microscope (CLM).**Specimen capillaries were
1078 transferred cryogenically to a home-built cryogenic spinning disk confocal fluorescence
1079 microscope [4]. Confocal scanning and detection were achieved using a commercial dual spinning
1080 disk head (CSU-X1, Yokogawa, Tokyo, Japan). During imaging, the illumination wavelength was
1081 selected with an acousto-optical tunable filter (AOTF) using an integrated system (Andor Laser
1082 Combiner, Model LC-501A).

1083 **Experimental measurement of the CLM point spread function.**The point spread function of
1084 the cryogenic confocal light microscope was calculated by the methods described in [5].

1085 **Acquisition of Cryogenic Fluorescence Tomography data.** Cryopreserved specimen capillaries
1086 were cryo-transferred to the CLM and aligned with respect to the rotation axis. Through-focus, or

1087 “z-stacks” were taken using a step size of 0.78 μm. For fluorescence tomography, the capillary
1088 was rotated about an axis normal to the objective lens using a motorized goniometer driven by
1089 custom LabView code (National Instruments Corporation, Austin, TX). Each tomographic data
1090 series consisted of 37 through-focus stacks (0° through 360° measured at 10° increments). Once
1091 measurements were completed, the capillary was cryo-transferred back to liquid nitrogen storage
1092 using the cryo-transfer device [5].

1093 **Alignment of through-focus fluorescence stacks using fluorescence fiducials.**Well-isolated
1094 fluorescent fiducials were chosen manually from the raw fluorescence stacks and a three-
1095 dimensional centroid algorithm refined the bead position to sub-pixel accuracy using the software
1096 package Amira (FEI). The fiducial coordinates were used to write a new image stack in MATLAB
1097 containing a spherically-symmetrical representation of the fiducials, which we termed the “fiducial
1098 model”. Six parameters were optimized for each alignment: three translations and three rotations
1099 (a rigid affine transformation). By limiting the search space to optimize correspondence between
1100 bead pairs that had been visually verified to be true fiducial correspondences, this alignment
1101 strategy was relatively fast and robust. The entire fluorescence fiducial alignment optimization
1102 process was visualized in Amira. Visualization was helpful for inspecting the results and
1103 troubleshooting rare cases where the optimization settled into a local maximum that was obviously
1104 not the real solution.

1105 **Fluorescence tomographic reconstruction and deconvolution.** Preprocessed, aligned through-
1106 focus stacks were reconstructed into a single object by simply summing the through-focus datasets
1107 (Amira). The effective PSF for tomographic imaging in a specimen capillary was used as the
1108 convolution kernel to deconvolve the fluorescence reconstruction. We used an iterative function

1109 for the deconvolution. The algorithm found the fluorophore distribution that was most likely,
1110 assuming the PSF was spatially invariant, and that image formation followed Poisson statistics.

1111 **Soft x-ray data collection and reconstruction.** Specimens were imaged using a transmission soft
1112 x-ray microscope, operated by the National Center for X-ray Tomography (NCXT), at the
1113 Advanced Light Source of Lawrence Berkeley National Laboratory and reconstructed according
1114 to previously published protocols.

1115 **Correlated Imaging.** Co-alignment of cryogenic fluorescence and soft x-ray tomographic
1116 reconstructions using joint fiducials

1117 Joint fiducials - red fluorescent polystyrene microspheres - visible in both light- and soft x-ray
1118 images were used to guide overlay of the two data types. The alignment process was optimized by
1119 converting the raw fluorescence into a bead model and aligning the fluorescent bead model to the
1120 x-ray reconstruction of the beads using an iterative optimization of the overlay.

1121 **Identification of JUNQ/IPOD in soft x-ray reconstructions.** Segmentation is the process of
1122 computationally isolating, visualizing, and quantifying specific cellular components in a
1123 tomographic reconstruction. Each voxel in an SXT reconstruction is a direct measurement of the
1124 soft x-ray Linear Absorption Coefficient (LAC) at the corresponding location in the cell.
1125 Attenuation of the illumination by the specimen follows Beer's Law. Hence, the LAC values for
1126 identical sized voxels depends solely on the concentration and composition of biomolecules
1127 present. Consequently, water has an order of magnitude lower LAC than carbon-containing
1128 molecules, such as lipids and proteins. LAC values for homogeneous solutions of isolated
1129 biomolecules can also be calculated using tables of known absorption coefficients. For example,
1130 pure water in the form of ice has a calculated LAC of 0.109 μm^{-1} whereas a model protein with

1131 the chemical composition $C_{94}H_{139}N_{24}O_{31}S$ was calculated to have a theoretical LAC of 1.35μm^{-1}
1132 [6]. In practice, most of the voxels in a 50 nm resolution SXT reconstruction of a cell will contain a
1133 heterogeneous mixture of biomolecules. Using SXT data acquired at a single wavelength it is not
1134 possible to distinguish the precise chemical species present. However, at this level of spatial
1135 resolution organelles and other sub-cellular structures are sufficiently similar in their biochemical
1136 composition to allow them to be readily identified from the surrounding cell contents. The
1137 relatively high water content in vacuoles makes them readily distinguishable from organelles with
1138 a greater density of biomolecules, for example, nuclei and mitochondria. Even relatively small
1139 variations in organelle LAC can be distinguished, for example, the boundaries between nuclei and
1140 nucleoli are very clear, as is the distinction between euchromatin and heterochromatin domains in
1141 the nucleus. LACs were calculated, and cells segmented using the protocols describe in complete
1142 detail in [3].

1143 Segmentation of the Hsp104-GFP reconstructions, in particular the assignment of the volumes as
1144 JUNQ and IPOD, were guided by correlative fluorescence signal. In other strains, JUNQ and/or
1145 IPOD were assigned based on LAC values established in the Hsp104-GFP study.

1146 **Western blot.** Yeast cultures were grown to mid- log-phase in synthetic complete medium (yeast
1147 nitrogen base, ammonium sulfate, amino acids, 2% raffinose) lacking uracil. Cultures were then
1148 diluted to an OD_{600} of 0.2 in galactose medium (synthetic complete medium with 2% galactose
1149 and 2% raffinose) and grown to an OD_{600} of 0.8. Cultures were then pelleted and resuspended in
1150 glucose medium (synthetic complete medium with 2% glucose) and incubated at either 30 or 37
1151 °C as indicated for the duration of the shut off. Where indicated, cultures were shifted to 37 °C for
1152 1 hour prior to exchange into glucose medium and incubated at 37 °C for the duration of the
1153 glucose shut-off. Cells were pelleted, proteins were extracted with urea and SDS, and protein

1154 concentrations were measured with the bicinchoninic acid protein assay kit (Thermo Fisher
1155 Scientific). Equal amounts of total protein were resolved on Tris-glycine gels (Invitrogen) and
1156 transferred onto nitrocellulose membranes. GFP was detected with mouse anti-GFP antibodies
1157 (Roche), GAPDH was detected with rabbit anti-GAPHD (Genetex), and PGK was detected with
1158 rabbit anti-PGK antibodies (Thermo Fisher Scientific). Secondary antibodies were IRDye 800CW
1159 donkey anti-mouse or IRDye 680RD donkey anti-rabbit and were imaged using the LiCOR
1160 scanner and Image Studio Software.

1161 To assess vacuolar protein degradation, the same procedure as above was followed but the *pep4D*
1162 yeast were treated with 1mM PMSF (Research Products International) during the 37C incubation
1163 step. The samples were then collected and lysed as above. GFP and GAPDH were detected with
1164 the same primary antibodies, but the secondary antibodies were goat anti-mouse HRP conjugated
1165 antibody (Promega Cat #W4021) and goat anti-rabbit HRP conjugated antibody (Promega Cat #
1166 W4011). Blots were detected using Clarity Western ECL Substrate (Bio-Rad Cat# 1705061) and
1167 imaged using the GE Amersham Imager 600.

1168 **Drop test.** Yeast cultures were grown to OD_{600} of 0.6 in YPD or raffinose synthetic complete
1169 medium and then diluted to OD_{600} of 0.1. Four 10-fold serial dilutions were performed in H_2O.
1170 ~2uL of diluted cultures were spotted onto YPD, galactose, or glucose plates using the pin plater.
1171 Plates were incubated at indicated temperatures and imaged every 24 hours for 72 hours.

1172 **Nanobody purification and labeling.** GFP-nanobody was expressed in BL21 Rosetta2 pLysS
1173 cells (Novagen), and DsRed-nanobody (LAM4) was expressed in ArticExpress cells (Agilent
1174 Technologies) overnight at 17 °C and 12 °C respectively. Cells were pelleted (4000XG), washed
1175 with PBS containing 1 mM PMSF and pelleted again. Pellets were resuspended in column buffer
1176 (500 mM NaCl and 50 mM HEPES pH 8 or 50 mM $NaHCO_3$ pH 8.3) with complete protease

1177 inhibitors, PMSF, benzonase and 10 mM imidazole (Lysis buffer) and lysed using an emulsiflex.
1178 Lysates were cleared at 20,000XG for 30 minutes. Nanobodies were purified using nickel resin
1179 by passing cleared lysate over the resin, washing with lysis buffer, followed by column buffer, and
1180 elution with column buffer containing 300 mM imidazole. Elution was concentrated using an
1181 Amicon ultra 3 kD MWCO to less than 2 mL, and further purified by size exclusion using an
1182 SDX75 column (GE Healthcare) equilibrated with 500 mM NaCl, 50 mM $NaHCO_3$, 1 mM DTT.
1183 Labeling was performed by the addition of dyes at a molar ratio of 5:1 dye:nanobody using Alexa
1184 488 NHS (Thermo Fisher Scientific) for the GFP nanobody and Alexa 568 NHS (Thermo Fisher
1185 Scientific) for the DsRed nanobody. Labeling reactions were incubated 1 hr at room temperature
1186 and quenched by addition of Tris-HCl pH 8 to a final concentration of 100 mM. Labeled nanobody
1187 was separated from free dye by size exclusion using an SDX75 column.

1188 **GFP-nanobody cloning**. pDG402, a vector for expression of GFP-nanobody-TEV-6XHis was
1189 generated by PCR amplification of the GFP nanobody using the 5' primer (XbaI GFP nanobody)
1190 AATCTAGAATTTTGTTTAACTTTAAGAAGG and 3' primer (GS link TEV His nanobody)
1191 AAGGATCCTTATCAGTGATGATGGTGGTGATGGGACCCAGATCCACCCTGGAAGTAT
1192 AAATTCTCACCCGAACCTCCGGATGAGGAGACGGTGACCTGGG. The PCR product
1193 was cloned into the pST39 backbone [7] using XbaI and BamHI.

1194 **METHODS REFERENCES**

1195 1 Brickner, D. G., Light, W. & Brickner, J. H. Quantitative localization of chromosomal
1196 loci by immunofluorescence. *Methods Enzymol* **470**, 569-580, doi:10.1016/S0076-
1197 6879(10)70022-7 (2010).

1198 2 Woerner, A. C. *et al.* Cytoplasmic protein aggregates interfere with nucleocytoplasmic
1199 transport of protein and RNA. *Science* **351**, 173-176, doi:10.1126/science.aad2033 (2016).

1200 3 Parkinson, D. Y. *et al.* Nanoimaging cells using soft X-ray tomography. *Methods Mol*
1201 *Biol* **950**, 457-481, doi:10.1007/978-1-62703-137-0_25 (2013).

1202 4 Le Gros, M. A., McDermott, G., Uchida, M., Knoechel, C. G. & Larabell, C. A. High-
1203 aperture cryogenic light microscopy. *J Microsc* **235**, 1-8, doi:10.1111/j.1365-2818.2009.03184.x
1204 (2009).

1205 5 Le Gros, M. A. *et al.* Biological soft X-ray tomography on beamline 2.1 at the Advanced
1206 Light Source. *J Synchrotron Radiat* **21**, 1370-1377, doi:10.1107/s1600577514015033 (2014).

1207 6 Weiss, D. *et al.* Computed tomography of cryogenic biological specimens based on X-ray
1208 microscopic images. *Ultramicroscopy* **84**, 185-197, doi:10.1016/s0304-3991(00)00034-6 (2000).

1209 7 Tan, S. A modular polycistronic expression system for overexpressing protein complexes

1210 in Escherichia coli. *Protein Expr Purif* **21**, 224-234, doi:10.1006/prep.2000.1363 (2001).

1211 **ACKNOWLEDGMENTS**

1212 We thank support of NIH (GM05643319 and AG054407 to JF; F32NS086253 to ES) and Way
1213 Klingler Startup Funds from Marquette University (ES). F.M-P. was supported by The Pew Trusts
1214 in the Biomedical Sciences postdoctoral Award (00034104). Cryo-SXT data were acquired at the
1215 Advanced Light Source of Lawrence Berkeley National Laboratory, a U.S. DOE Office of Science
1216 User Facility. The National Center for X-ray Tomography is supported by NIH (P41GM103445)
1217 and DOE BER (DE-AC02-5CH11231). CAL and MAL were supported by the Gordon and Betty
1218 Moore Foundation Award #3497. The Stanford Cell Sciences Imaging Facility is supported in part
1219 by Award Number 1S10OD01227601 from the National Center for Research Resources (NCRR).
1220 We thank Jon Mulholland and Youngbin Lim from the CSIF for training on the SIM. We are
1221 grateful to Michael Rosbash (Brandeis University), Susan Wente (Vanderbilt University), Kiran
1222 Madura (Rutgers University), and Patrick Lusk (Yale School of Medicine) for providing yeast
1223 strains and Karsten Weis (ETH Zurich), Jodi Nunnari (University of California, Davis), and
1224 Michael P. Rout (Rockefeller University) for plasmids. We thank Katharine Ullman (University
1225 of Utah), Adam Frost (Altos Lab) and Lisbeth Veenhoff (University of Groningen) for discussions
1226 and advice. We are grateful to Carson Trail for support in microscopy data analysis, Margaret

Wangeline for assisting with the 2xKeima cloning, Joan Steffan (UC Irvine), Kelly Rainbolt (Stanford University) for discussions and comments on the manuscript, Felipe Serrano for assisting on Figure 8, and the Frydman lab for advice and discussions.

AUTHOR CONTRIBUTIONS

JF, ES conceived the project; ES and F. M-P carried out all experiments; J-HC collected and processed cryo-SXT data; GM carried out cryo-SXT data analysis and modelling; MLG performed cryo-fluorescence data acquisition and correlation with cryo-SXT data and built the microscope used for these experiments. PD analyzed particle tracking data and assisted on statistical analyses. DG cloned the NLS- and NES- luciferase and VHL plasmids. DG and F. M-P generated, purified and labeled the GFP and RFP nanobodies. ES, F. M-P and JF wrote the MS. All authors commented on the final version. JF directed the project.

DECLARATION OF INTERESTS

The authors declare no competing interests.

ADDITIONAL INFORMATION

Supplementary information is available for this paper.

Correspondence and requests for materials should be addressed to Judith Frydman jfrydman@stanford.edu

EXTENDED DATA FIGURE LEGENDS

1246 **Figure ED1: Spatial sequestration occurs during different types of stress with different**

1247 **client proteins.**

1248 (a) Western blot analyses of Gal Shut-off assays showing the clearance of NLS-LuciTs (top) and

1249 NES-LuciTs (bottom) with and without proteasome impairment by 50uM Bortezomib. (b) Drop

1250 test of W303 yeast expressing model proteins without heat shock at 30C (left), with heat shock at

1251 37 °C (middle), and without expression of the plasmids (right). (c) Representative Structured

1252 Illumination super-resolution microscopy images taken of cells expressing NLS-VHL (left) or

1253 NES-VHL (right) after 120 minutes at 37 °C and treated with 100μM MG132. NLS-LuciTs is

1254 shown in green, NES-LuciTs in purple, nuclear pores in gold and Hoechst counterstain in blue.

1255 Scale bars are 1μm.

1256

1257 **Figure ED2: The effect of blocking nucleocytoplasmic transport on Ubc9Ts clearance.**
1258 (a) Quantitation of the percentage of cells containing nuclear or cytoplasmic inclusions in WT
1259 yeast expressing Ubc9Ts-EGFP after 120 minutes at 37 °C with and without treatment with
1260 100μM MG132. A minimum of 500 cells per condition from 3 biologically independent
1261 experiments were counted and Student's t-tests were performed comparing the WT yeast without
1262 MG132 treatment to WT yeast with MG132 treatment using Prism software. P values were
1263 adjusted using two-stage linear step-up procedure of Benjamini, Krieger and Yekutieli with a Q
1264 of 5%. Adjusted P value for nuclear no MG132 vs. +MG132 is 0.0035 and cytoplasmic no
1265 MG132 vs. +MG132 is 0.0011. (b) Representative Structured Illumination super-resolution
1266 microscopy images taken of cells expressing GFP-VHL after 2 hr at 37 °C with DMSO (left) or
1267 with 100μM MG132 (right) treatment. VHL is shown in green, nuclear pores in gold, and
1268 Hoechst counterstain in blue. Scale bars are 1μm. (c) (left) Schematic illustrating the *nup116-5*
1269 yeast have sealed nuclear pores at 37 °C, thus blocking nucleocytoplasmic trafficking. (right)
1270 There is no significant difference in half-life between WT and *nup116-5* yeast. (d) (left)
1271 Schematic illustrating the *sts1-2* yeast do not translocate proteasomes to the nucleus at 37 °C.
1272 (right) There is no significant difference in half-life between WT and *sts1-2* yeast. (c and d)
1273 Levels of EGFP were quantified from 3 biologically independent experiments. Half-life was
1274 calculated using Prism.

1275

1276 **Figure ED3: INQ-JUNQ homing does not occur at the LINC, nucleolus, or involve FG**
1277 **repeats of the nuclear pore central channel.**
1278 (a) Graph of the X-Y positions of the INQ and JUNQ compartments by particle tracking of
1279 inclusions from cell shown in Figure 2a over the time course of the experiment. (b)
1280 Representative confocal image taken of cells co-expressing NLS-EGFP-VHL and NES-DsRed-
1281 VHL after 2 hr at 37 °C and treated with 100μM MG132. NLS-fusion proteins are shown in
1282 green, NES-fusion proteins in purple, nuclear pores in gold, and Hoechst counterstain in blue.
1283 Scale bar is 1μm. (c) Representative confocal fluorescence microscopy images taken of cells co-
1284 expressing NLS-EGFP-LuciTs and NES-DsRed-LuciTs (left) after 2 hr at 37 °C and treated with
1285 100μM MG132. NLS-LuciTs is shown in green, NES-LuciTs in purple, nucleolus (Nsr1) in gold
1286 and Hoechst counterstain in blue. (right) Line intensity profile showing distance between
1287 nucleolus and homed INQ/JUNQ. Scale bars are 1μm. (d) (left) schematic of Mps3 component
1288 of LINC complex linking inner and outer nuclear membranes. (right) Representative widefield
1289 fluorescence microscopy images taken of cells co-expressing endogenously tagged Mps3-EGFP
1290 and NES-DsRed-LuciTs after 120 minutes at 37 °C with and without treatment with 100μM
1291 MG132. White arrowheads indicate locations of Mps3 puncta while yellow arrowheads indicate
1292 NES-LuciTs puncta. Scale bars are 1μm. (e) WT (top) and *nupΔFG* (bottom) cells co-expressing
1293 NLS-LuciTs and NES-LuciTs were shifted to 37 °C and monitored by live cell time-lapse
1294 fluorescence microscopy for the times shown. Scale bars are 1μm.

1295

1296 **Figure ED4: Detailed representation of the cryo-SXT workflow and interactions between**
1297 **mitochondria and cytoplasmic PQC compartments.**
1298 (a) Optical path through the specimen. Key: COL, cryogenic objective lens; SS, specimen stage;
1299 SP, specimen port; MG, motorized goniometer; CIM, cryogenic immersion fluid; CCL, low
1300 magnification cryogenic objective; CS, cryogenic specimen; CIE, cryogenic imaging
1301 environment; AP, adapter port; AW, a heated, angled anti-reflection window. (b) Alignment of
1302 fluorescence and soft x-ray tomographic data using fiducial markers. (c) A representative
1303 confocal image of the spatial relationship between the INQ and nucleolus. NLS-LuciTs (INQ) is
1304 shown in green, nucleolus in gold, and Hoechst counterstain in blue. Scale bar is 1μm. (d) The
1305 interaction between mitochondria and cytoplasmic inclusions is also seen by fluorescence
1306 confocal microscopy in a representative image of a cell co-expressing mito-GFP and NES-RFP-
1307 LuciTs. NES-LuciTs is shown in purple, mitochondria in cyan, and Hoechst counterstain in blue.
1308 Scale bar is 1μm. (e) Representative confocal fluorescence microscopy images taken of WT,
1309 fission mutants (*dnm1Δ* and *fis1Δ*) and fusion mutant (*fzo1Δ* and *ugo1Δ*) cells expressing mito-
1310 GFP and NES-DsRed-LuciTs after 120 minutes at 37 °C and treated with 100μM MG132. Mito-
1311 GFP is shown in cyan, NES-LuciTs in purple, and Hoechst counterstain in blue. Scale bars are
1312 1μm.

1313

1314 **Figure ED5: NVJ -mediated clearance of misfolded proteins.**

1315 (a) Endogenously tagged Nvj1-GFP yeast expressing Ubc9Ts-ChFP were shifted to 37 °C and
1316 monitored by live cell time-lapse fluorescence microscopy for the times shown. White
1317 arrowheads indicate locations of Nvj1 puncta while yellow arrowheads indicate Ubc9Ts-ChFP
1318 puncta. Scale bar is 1µm. (b) WT (top) and *nvj1*Δ (bottom) cells co-expressing NLS-LuciTs and
1319 NES-LuciTs were treated with 100µM MG132 and shifted to 37 °C for 30 mins to preform
1320 inclusions. Cells were then placed in media containing 50mg/ml cycloheximide (CHX) and
1321 100µM MG132 at 37 °C and monitored by live cell time-lapse fluorescence microscopy for the
1322 times shown. Scale bars are 1µm. (c,d) Quantitation of the percentage of cells containing
1323 cytoplasmic inclusions in WT, *nvj1Δ*, and *vac8Δ* yeast co-expressing NLS-EGFP-LuciTs (c) and
1324 NES-DsRed-LuciTs (d) after 2 hr at 37 °C with and without treatment with 100µM MG132. A
1325 minimum of 500 cells per condition from 3 biologically independent experiments were counted
1326 and unpaired Student's t-tests were performed comparing the deletion strains to WT with or
1327 without MG132 treatment were compared. P values were adjusted using two-stage linear step-up
1328 procedure of Benjamini, Krieger and Yekutieli with a Q of 5%. (c) %. Adjusted P value for WT
1329 vs *nvj1Δ* no MG132 is 0.0205, WT vs *nvj1Δ* +MG132 is 0.2357, WT vs *vac8Δ* no MG132 is
1330 0.0406, WT vs *vac8Δ* +MG132 is 0.8974, and WT no MG132 vs WT +MG132 is 0.0239. (d)
1331 Adjusted P value for WT vs *nvj1Δ* no MG132 is 0.013, WT vs *nvj1Δ* +MG132 is 0.013, WT vs
1332 *vac8Δ* no MG132 is 0.0008, WT vs *vac8Δ* +MG132 is 0.0447, and WT no MG132 vs WT
1333 +MG132 is 0.0005. (e) Levels of EGFP after 1 hour at 37 °C were measured from Quantitative
1334 Western blots (mean ± s.e.m. from three biologically independent experiments). WT and nvj1Δ
1335 yeast were compared using an unpaired Student's t-test resulting in a P value of 0.0043 for WT
1336 vs nvj1Δ NLS-LuciTs and NES-LuciTs P value is 0.0183. Statistics were performed using Prism.

1337

1338 **Figure ED6: ESCRT involvement in the clearance of misfolded proteins.**

1339 (a) Representative confocal images of WT yeast co-expressing Chm7-EGFP and either NLS-
1340 EGFP-LuciTs (left) or NES-DsRed-LuciTs (right) after 120 minutes at 37 °C and treated with
1341 100μM MG132. Chm7 is shown in teal and remains diffuse throughout the cell, NLS-EGFP-
1342 LuciTs in green, NES-DsRed-LuciTs in purple, nuclear pores in gold and Hoechst counterstain
1343 in blue. Scale bar is 1μm. (b) Representative confocal images of WT and *vps23Δ* ,
1344 *vps34Δ,* and *vps15Δ* yeast co-expressing NLS-EGFP-LuciTs and NES-DsRed-LuciTs after 2 hr
1345 at 37 °C and treated with 100μM MG132. NLS-EGFP-LuciTs is shown in green, NES-DsRed-
1346 LuciTs in purple, nuclear pores in gold, and Hoechst counterstain in blue. Insets show the
1347 budding INQ encapsulated by nuclear pores. Scale bars are 1μm. Same data as shown in Figure
1348 6c, but with the green channel separated to clearly detail the colocalization with the cytoplasmic
1349 protein.

1350 **Figure ED7: Vacuole-mediated clearance of INQ and JUNQ.**

1351 (a) Representative images of WT cells expressing NES-2xKeima-LuciTs after 2 hr incubation at
1352 37 °C with 100μM MG132. Over time, fluorescence is seen with excitation in the 589nm channel
1353 indicating the NLS-LuciTs has encountered an acidic environment. Insets show the transition
1354 from green to red and a structure leaving the inclusion that is fully red. Scale bars are 5 uM. Same
1355 data shown in Figure 7d, but with more time points and a larger field of view in the images. (b)
1356 WT cells expressing NES-2xKeima-LuciTs after 85 min incubation at 37 °C with 100μM
1357 MG132. (c) Longer exposure of the blot shown in Figure 7f to highlight the difference in the
1358 number and pattern of the GFP bands in the WT vs *pep4Δ* cells. (d) Levels of EGFP at time 0

1359 were measured from Quantitative Western blots such as those shown in Figure 7e,f (mean ±
1360 s.e.m. from three biologically independent experiments). WT and *pep4Δ* yeast were compared
1361 using an unpaired Student's t-test without reaching statistical significance. (e) WT yeast
1362 expressing NLS-GFP-LuciTs were treated with 8uM of FM4-64 and incubated for 2hr at 37 °C
1363 with 100μM MG132. Cells were imaged every 30 sec for 90 mins. Scale bar is 1μm. Same data
1364 shown in Figure 7h, but only WT and with more timepoints during the entry into the vacuole.

1365

1366

1367 **Legends to movies**

1368 Movie 1. Live-cell time-lapse fluorescence microscopy of WT cells expressing NLS-LuciTs
1369 (left) or NES-LuciTs (right) at 37 °C, treated with 100μM MG132. Same data shown in stills in
1370 Figure 1c (left), d (right).

1371 Movie 2. Dynamic representation of the 3D reconstructions of the data shown in Figure 1e
1372 (left),g (right). Videos were created in Volocity.

1373 Movie 3. Dynamic representation of the 3D reconstructions of the data shown in Figure 2a (left),
1374 b (right). Videos were created in Volocity.

1375 Movie 4. Live-cell time-lapse fluorescence microscopy of the data shown in Figure 3a.

1376 Movie 5. Dynamic representation of the data shown in Figure 3b.

1377 Movie 6. Dynamic representation of the 3D reconstruction of the data shown in Figure 3c. Video
1378 was created in Volocity.

1379 Movie 7. Dynamic representation of the 3D reconstruction shown in Figure 4c. Video was
1380 created in Amira.

1381 Movie 8. Dynamic representation of the 3D reconstruction shown in Figure 4d,f. Video was
1382 created in Amira.

1383 Movie 9. Live-cell time-lapse fluorescence microscopy of the data shown in Figure 5a.

1384 Movie 10. Dynamic representation of the 3D reconstruction of the data shown in Figure 5c.
1385 Video was created in Volocity.

1386 Movie 11. Dynamic representation of the 3D reconstruction of the data shown in Figure 5b.
1387 Video was created in Volocity.

1388 Movie 12. Live-cell time-lapse fluorescence microscopy of the data shown in Figure 5f.

1389 Movie 13. Dynamic representation of the 3D reconstruction of the data shown in Figure 5e.
1390 Video was created in Volocity.

1391 Video 14. Live-cell time-lapse fluorescence microscopy of the WT cell data shown in Figure 5h.

1392 Video 15. Live-cell time-lapse fluorescence microscopy of the *nvj1Δ* cell data shown in Figure
1393 5h.

1394 Video 16. Live-cell time-lapse fluorescence microscopy of the *vps4Δ* cell data shown in Figure
1395 5h.

Sontag et al.
Figure 1

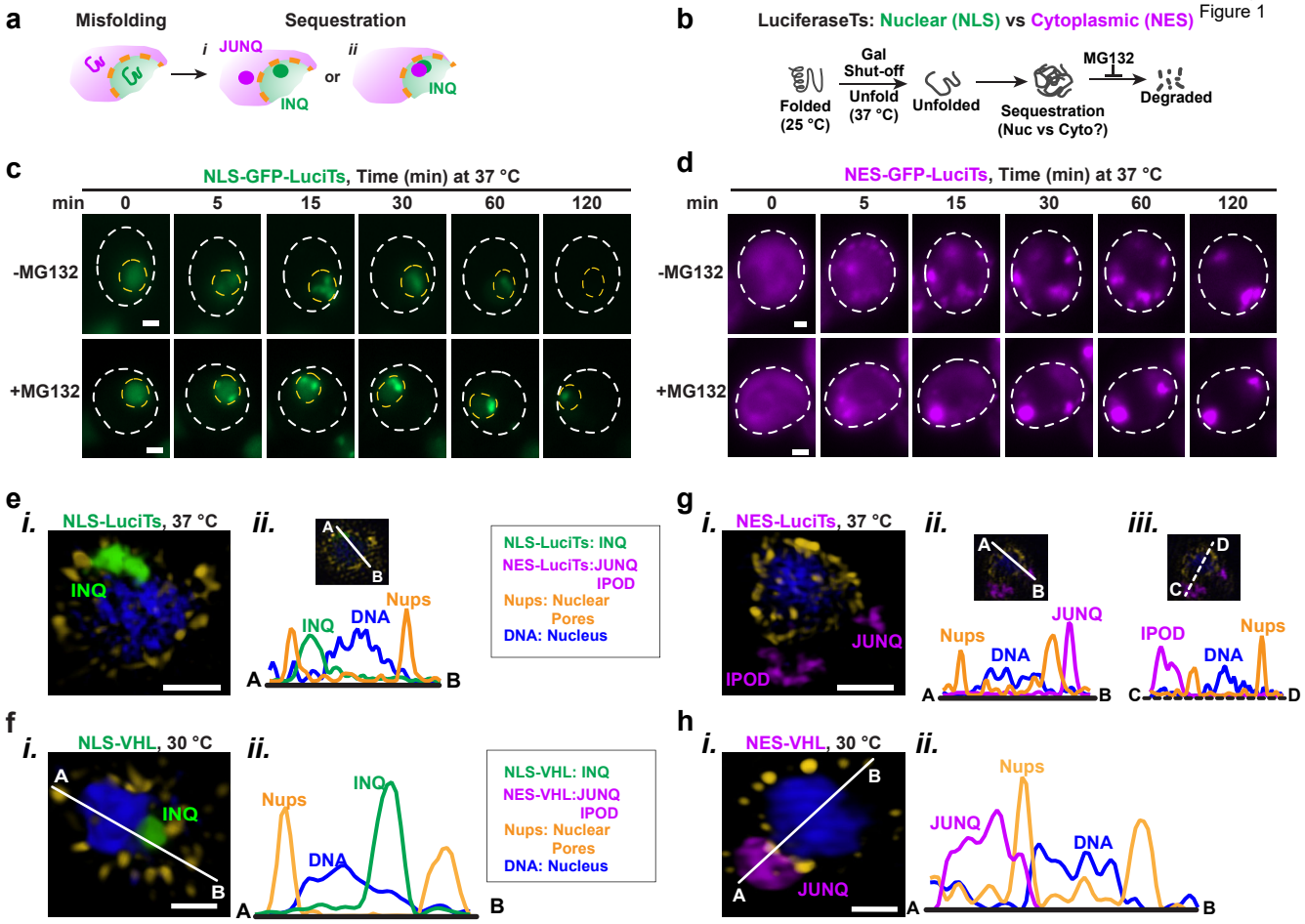

Sontag et al.
Figure 2

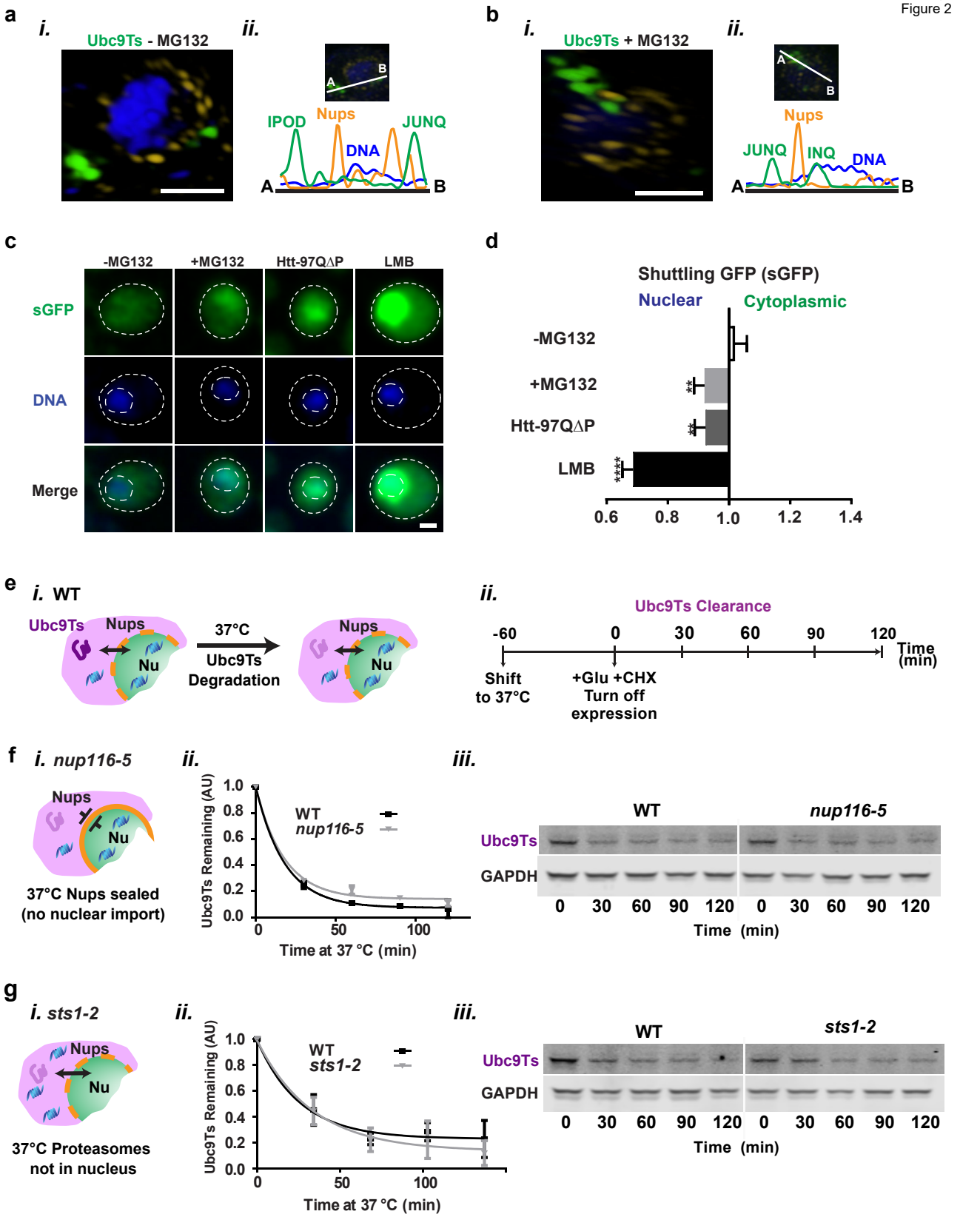

Sontag et al.
Figure 3

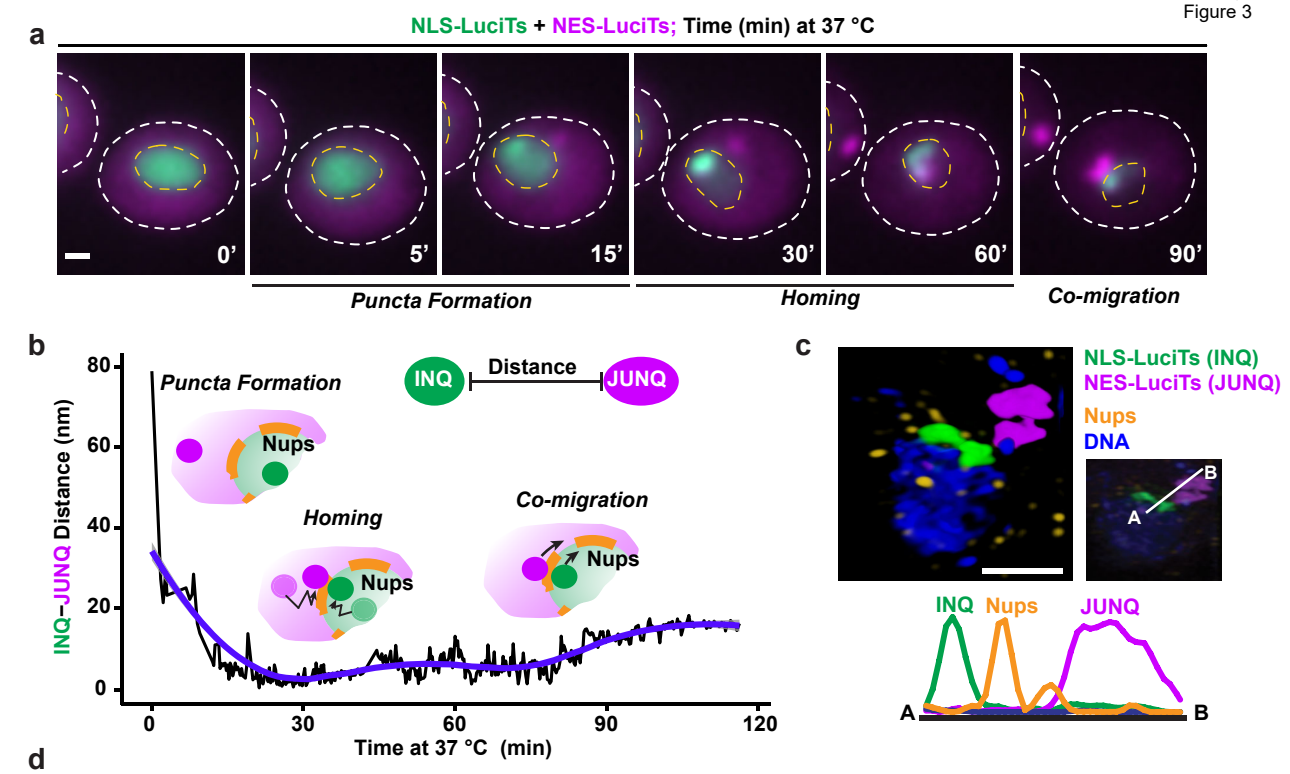

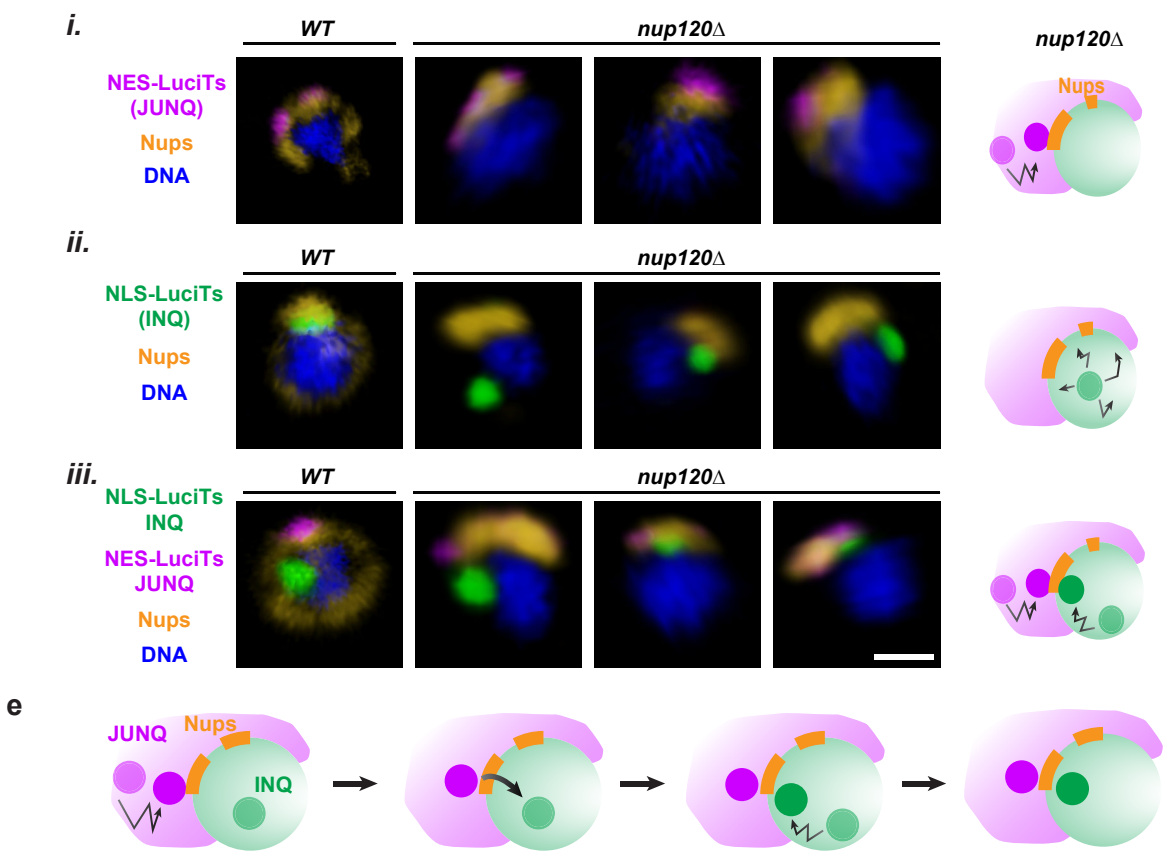

Sontag et al.
Figure 4

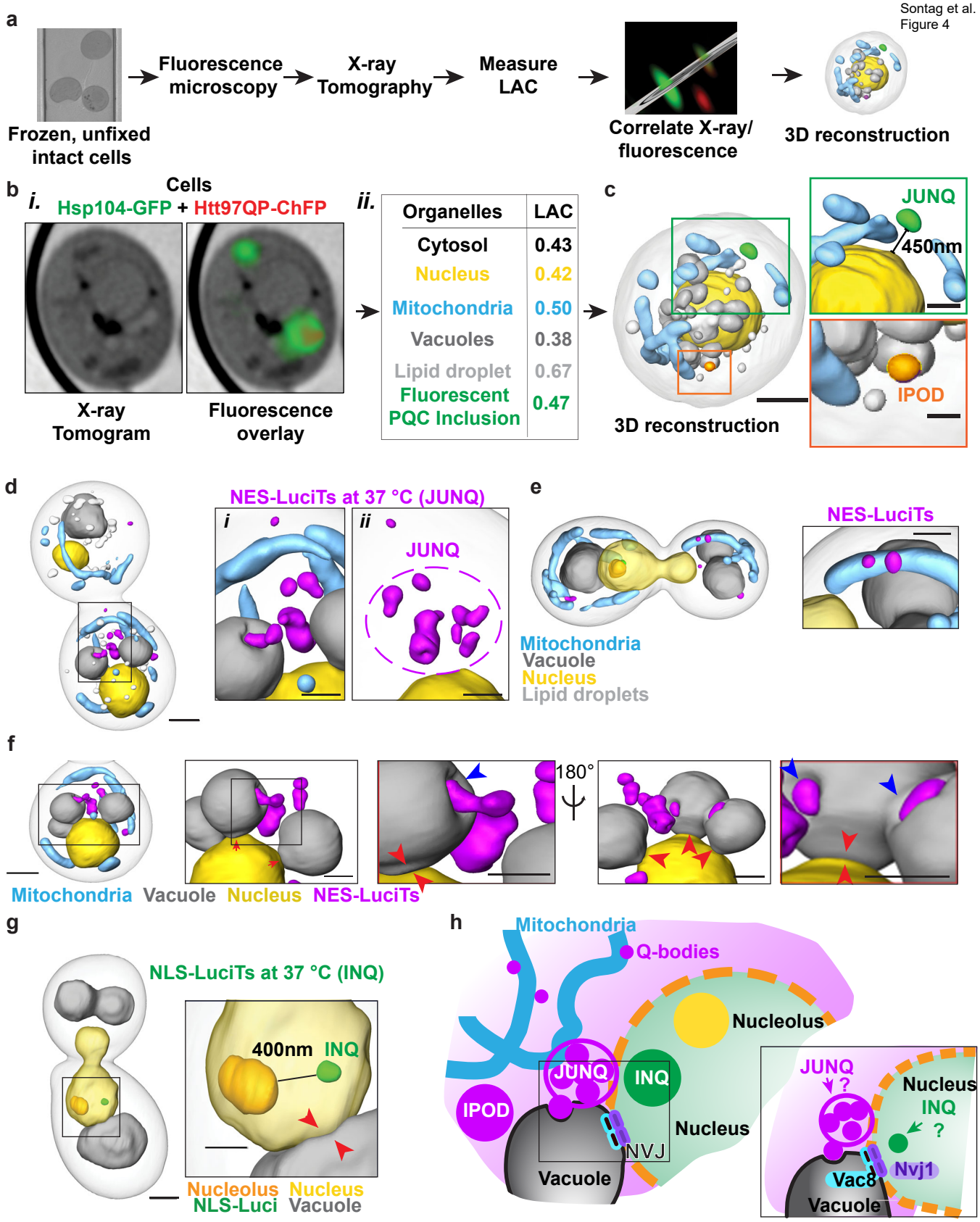

Sontag et al.
Figure 5

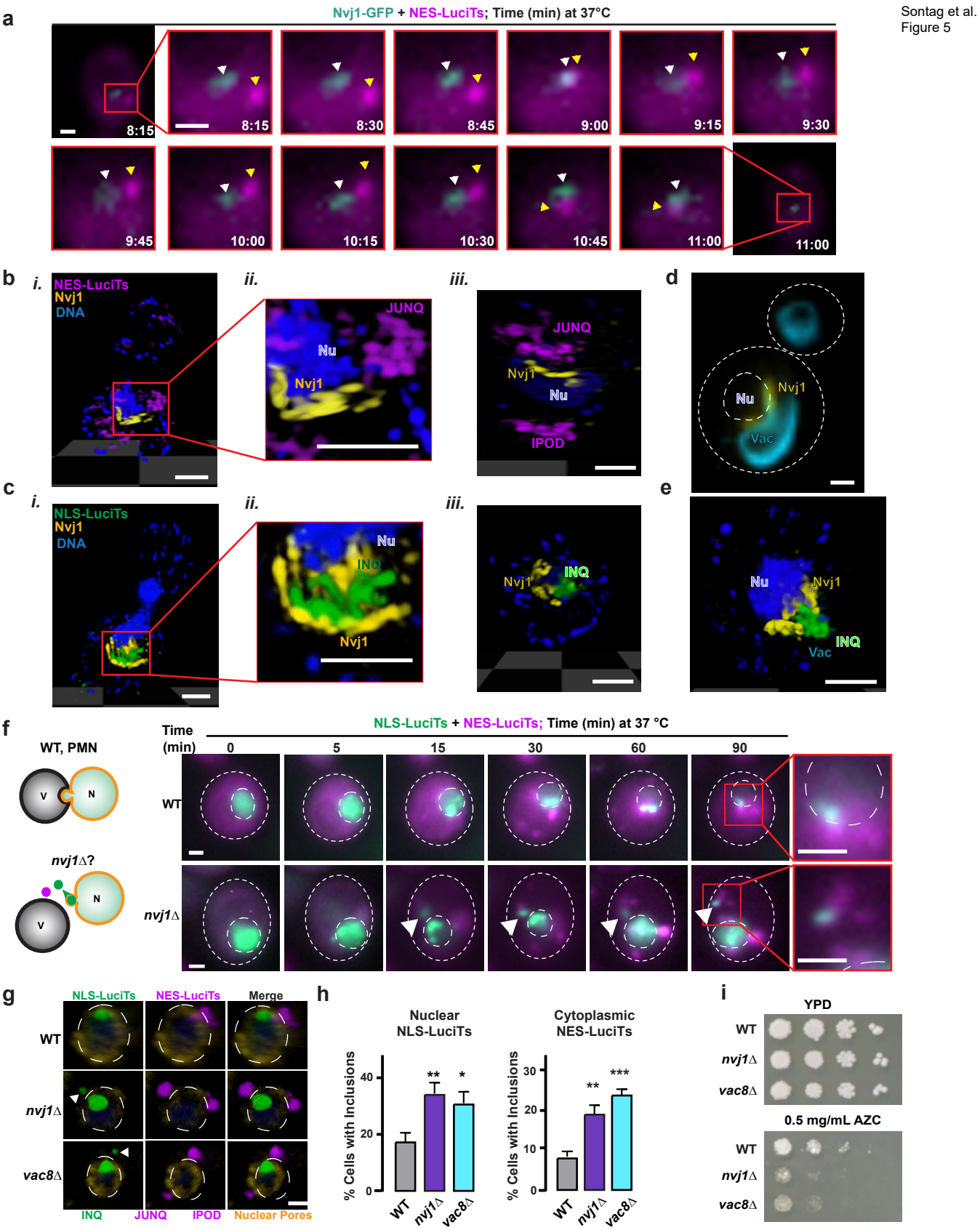

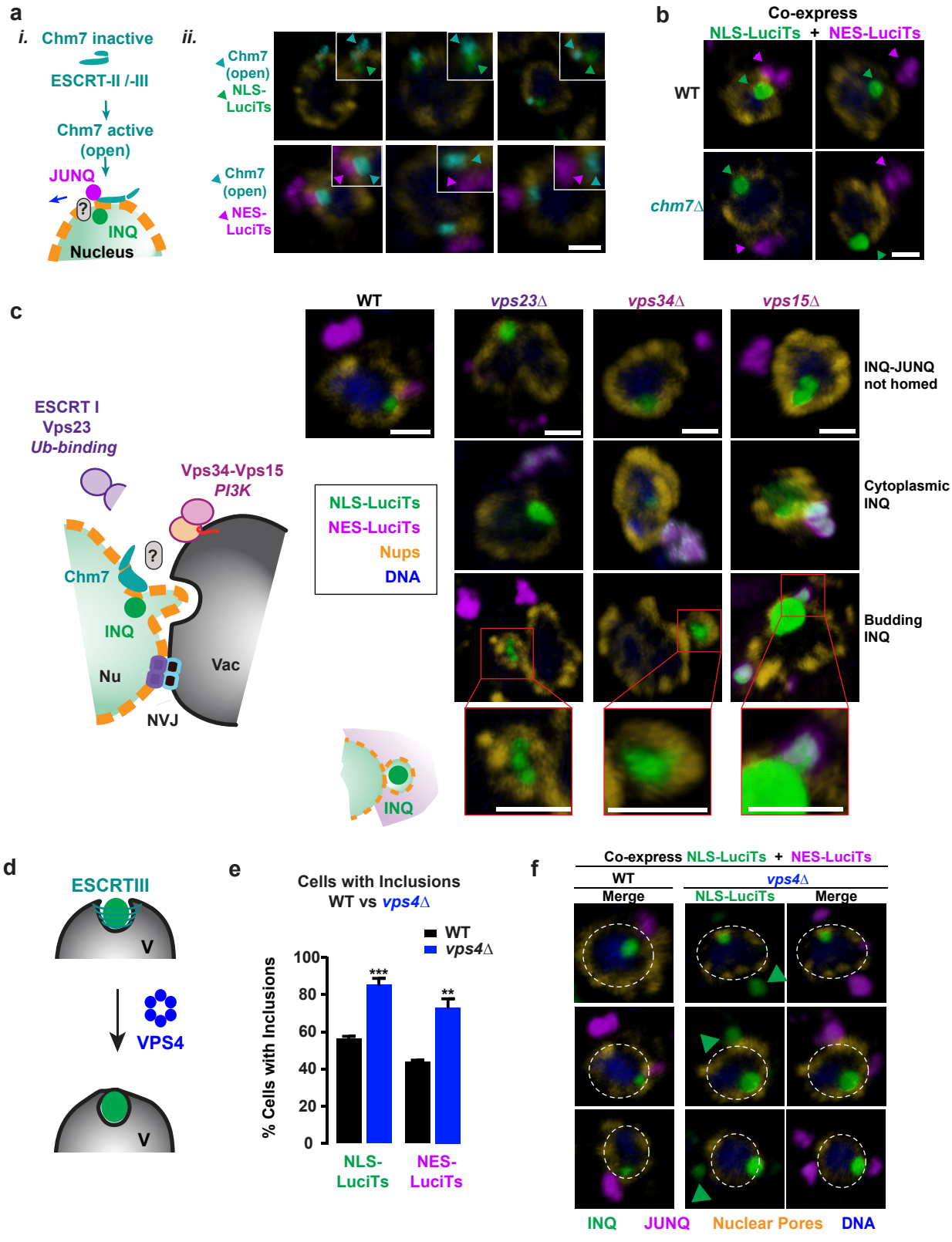
a
i.
Chm7 inactive
ESCRT-II /-III
Chm7 active
(open)
JUNQ
?
INQ
Nucleus
ii.
Chm7
(open)
NLS-
LuciTs
Chm7
(open)
NES-
LuciTs
b
Co-express
NLS-LuciTs + NES-LuciTs
WT
chm7Δ
c
ESCRT I
Vps23
Ub-binding
Vps34-Vps15
PI3K
Chm7
?
INQ
Nu
Vac
NVJ
WT
vps23Δ
vps34Δ
vps15Δ
INQ-JUNQ
not homed
Cytoplasmic
INQ
Budding
INQ
NLS-LuciTs
NES-LuciTs
Nups
DNA
INQ
d
ESCRTIII
V
VPS4
V
e
Cells with Inclusions
WT vs vps4Δ
WT
vps4Δ
% Cells with Inclusions
100
80
60
40
20
0
***
**
NLS-
LuciTs
NES-
LuciTs
f
Co-express NLS-LuciTs + NES-LuciTs
WT
vps4Δ
Merge
NLS-LuciTs
Merge
INQ
JUNQ
Nuclear Pores
DNA

Sontag et al.
Figure 7

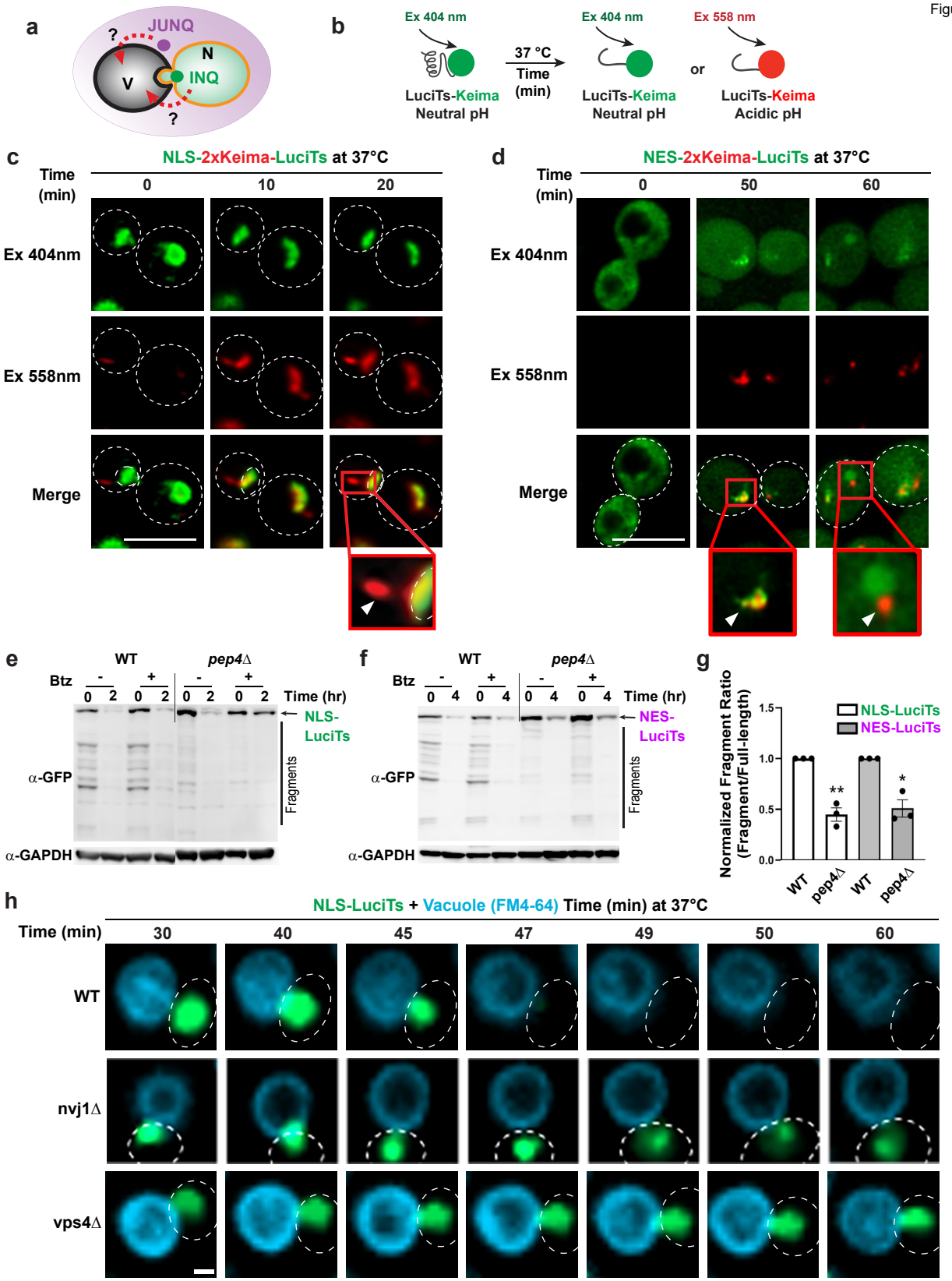

Sontag et al.
Figure 8

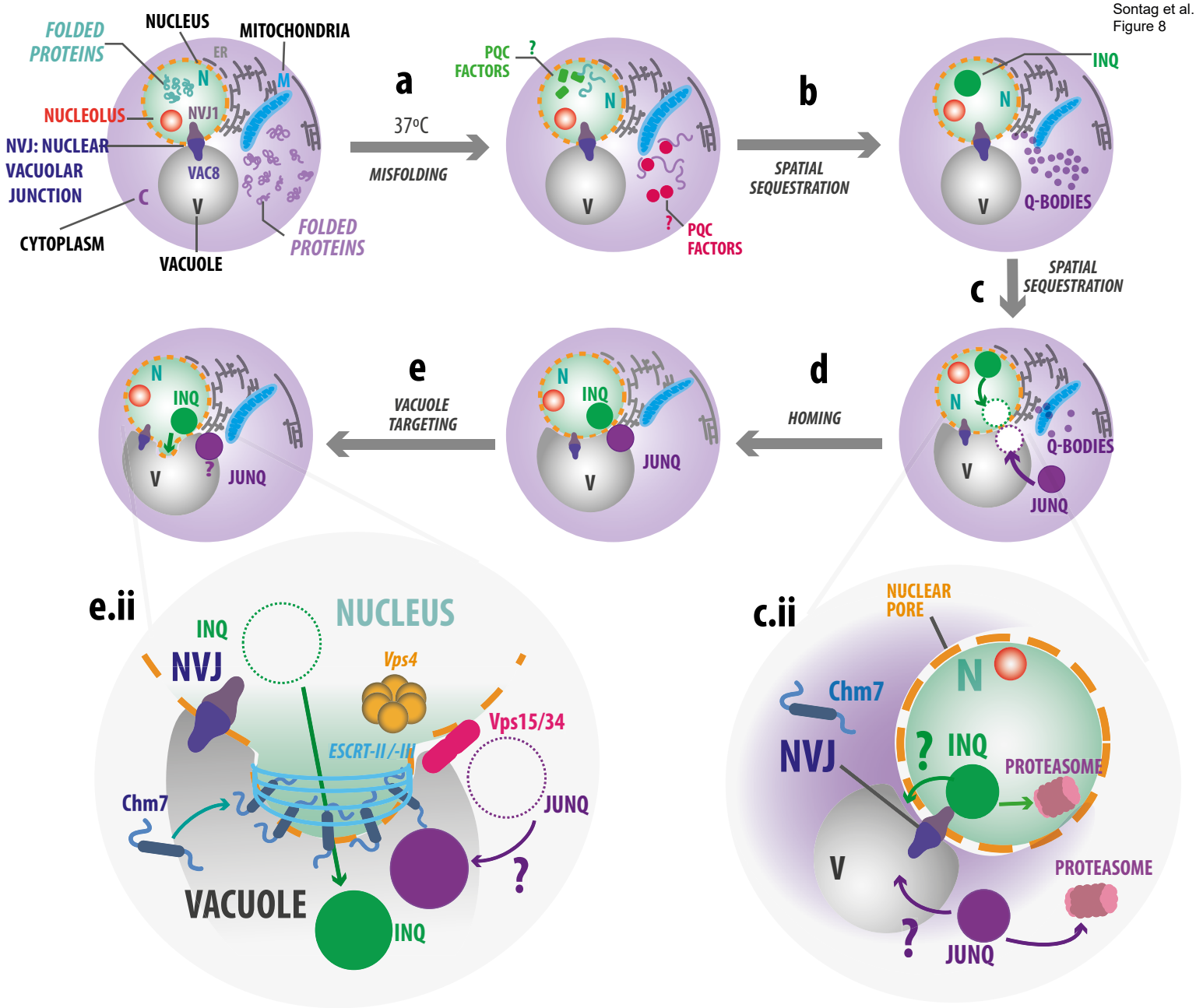

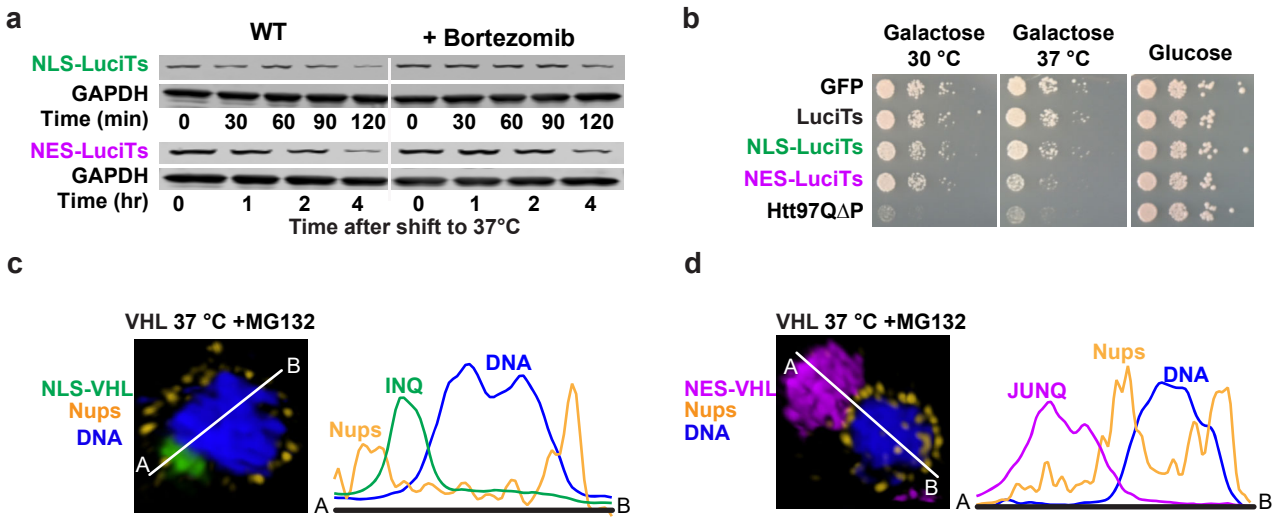
a
WT
+ Bortezomib
NLS-LuciTs
GAPDH
Time (min)
0 30 60 90 120 0 30 60 90 120
NES-LuciTs
GAPDH
Time (hr)
0 1 2 4 0 1 2 4
Time after shift to 37°C
b
Galactose 30 °C
Galactose 37 °C
Glucose
GFP
LuciTs
NLS-LuciTs
NES-LuciTs
Htt97QΔP
c
VHL 37 °C +MG132
NLS-VHL
Nups
DNA
A
B
INQ
DNA
Nups
d
VHL 37 °C +MG132
NES-VHL
Nups
DNA
JUNQ
Nups
DNA

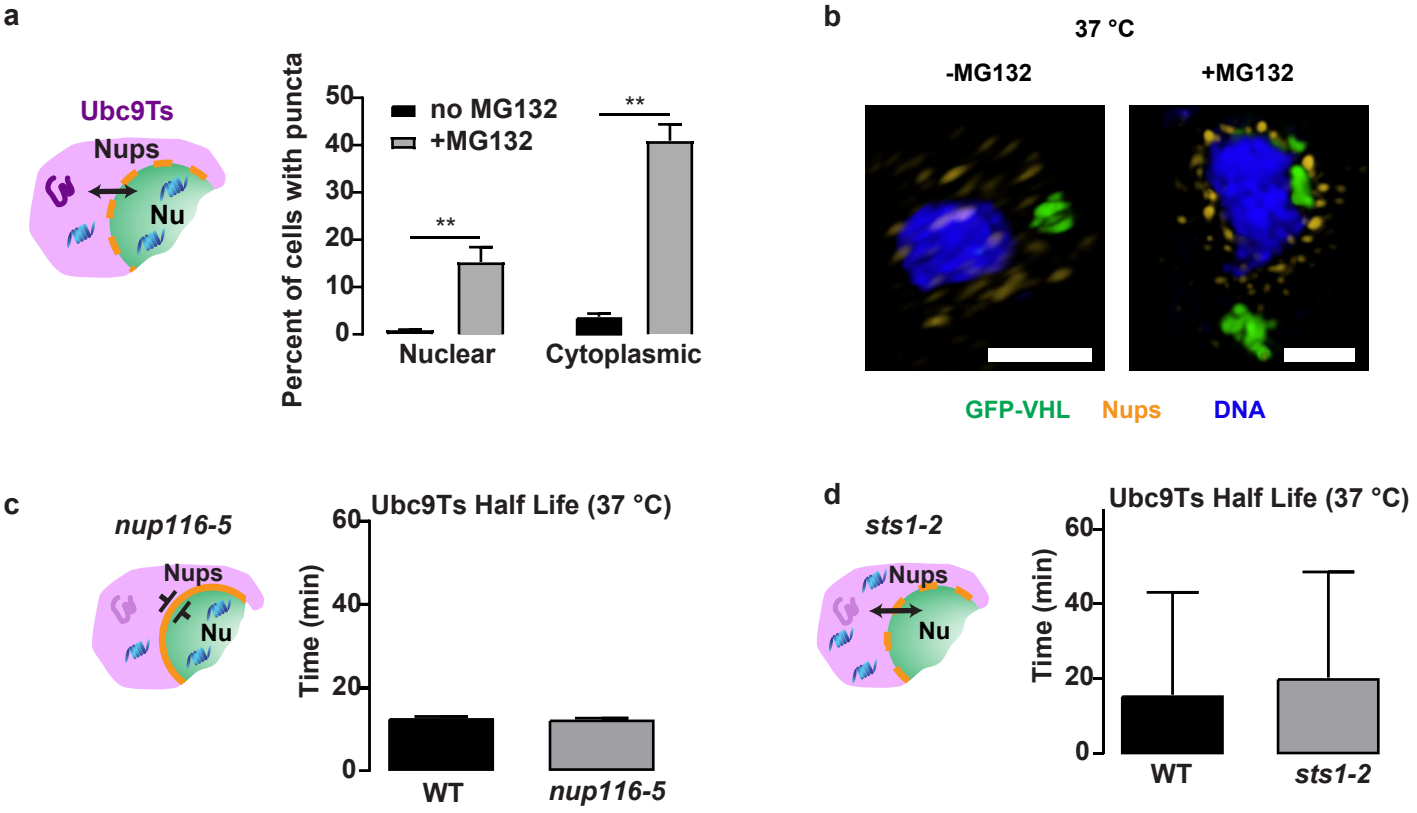
a
Ubc9Ts
Nups
Nu
Percent of cells with puncta
50
40
30
20
10
0
no MG132
+MG132
**
**
Nuclear
Cytoplasmic
b
37 °C
-MG132
+MG132
GFP-VHL
Nups
DNA
c
nup116-5
Nups
Nu
Ubc9Ts Half Life (37 °C)
Time (min)
60
40
20
0
WT
nup116-5
d
sts1-2
Nups
Nu
Ubc9Ts Half Life (37 °C)
Time (min)
60
40
20
0
WT
sts1-2

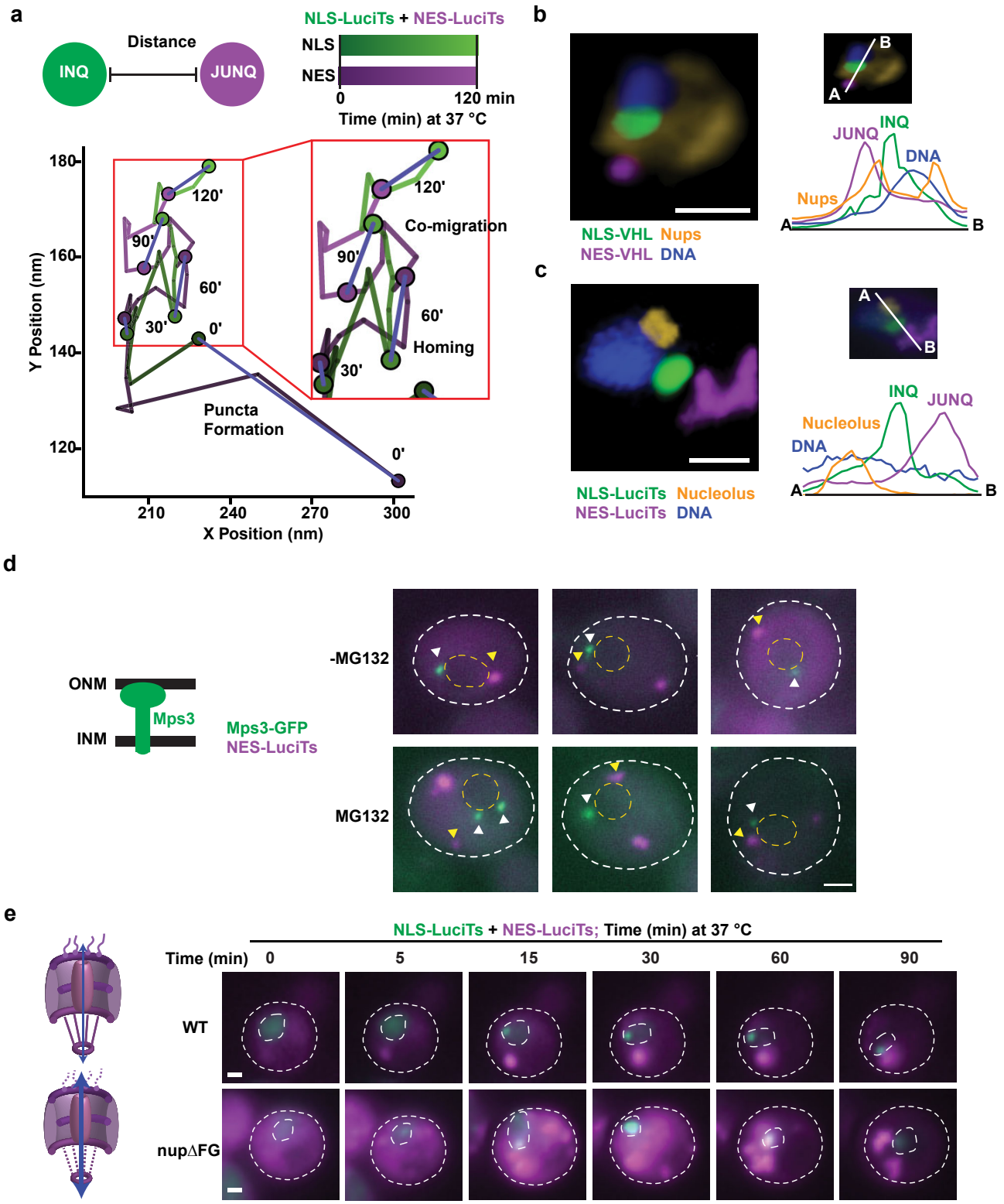
a
INQ
Distance
JUNQ
NLS-LuciTs + NES-LuciTs
NLS
NES
0
120 min
Time (min) at 37 °C
Y Position (nm)
X Position (nm)
180
160
140
120
210
240
270
300
120'
90'
60'
30'
0'
Co-migration
Homing
Puncta
Formation
b
NLS-VHL Nups
NES-VHL DNA
A
B
JUNQ
INQ
DNA
Nups
c
NLS-LuciTs Nucleolus
NES-LuciTs DNA
Nucleolus
d
ONM
INM
Mps3
Mps3-GFP
NES-LuciTs
-MG132
MG132
e
NLS-LuciTs + NES-LuciTs; Time (min) at 37 °C
Time (min)
0
5
15
30
60
90
WT
nupΔFG

Sontag et al.
Figure ED4

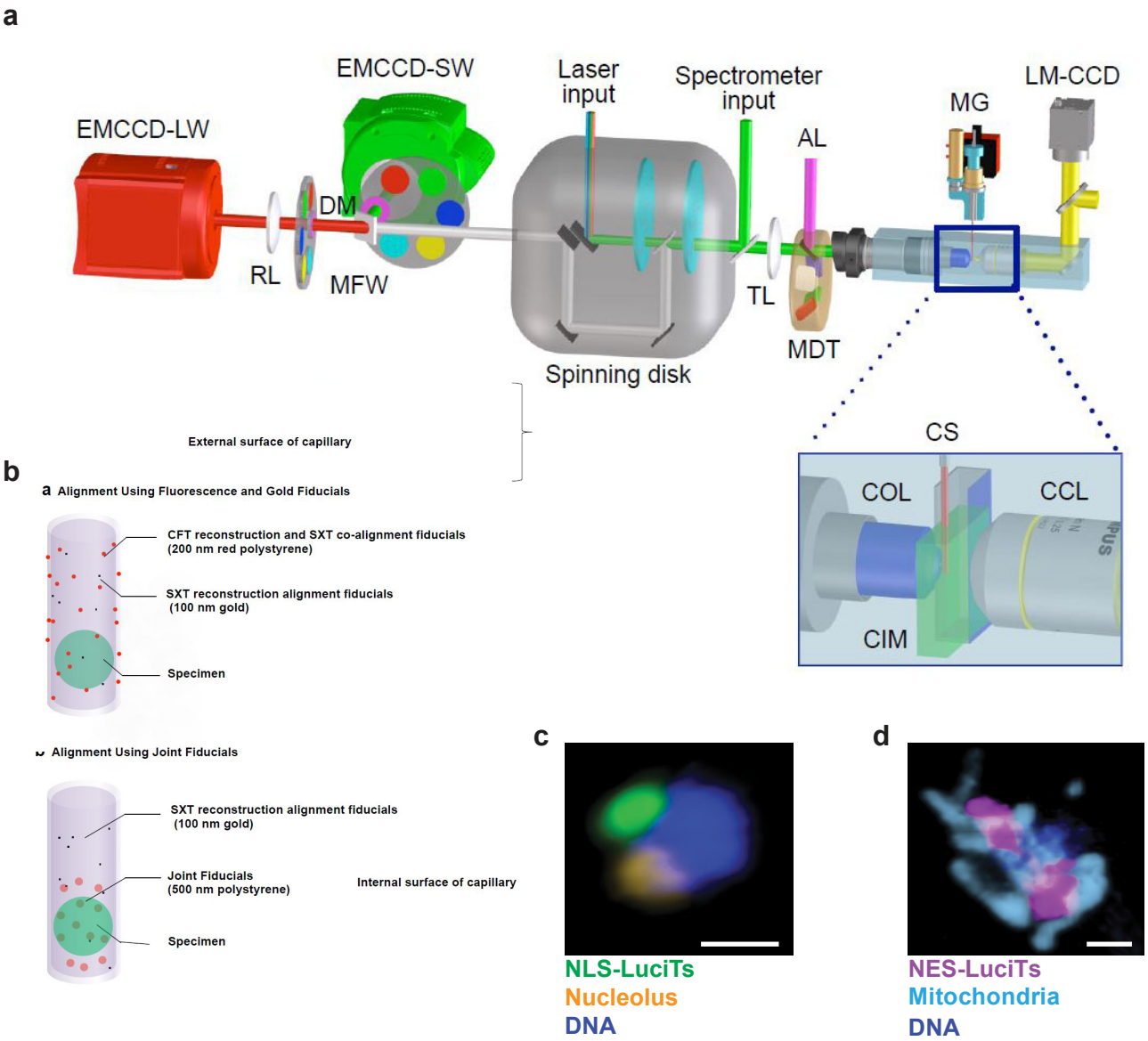

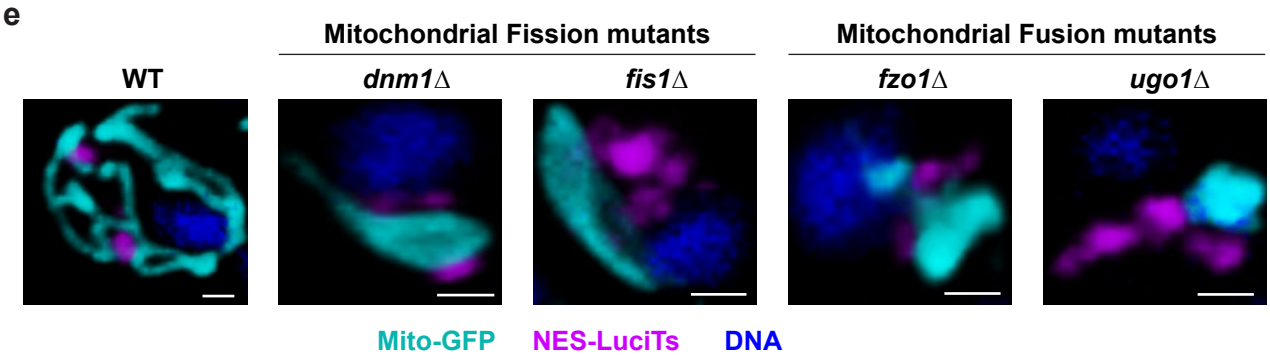

Sontag et al.
Figure ED5

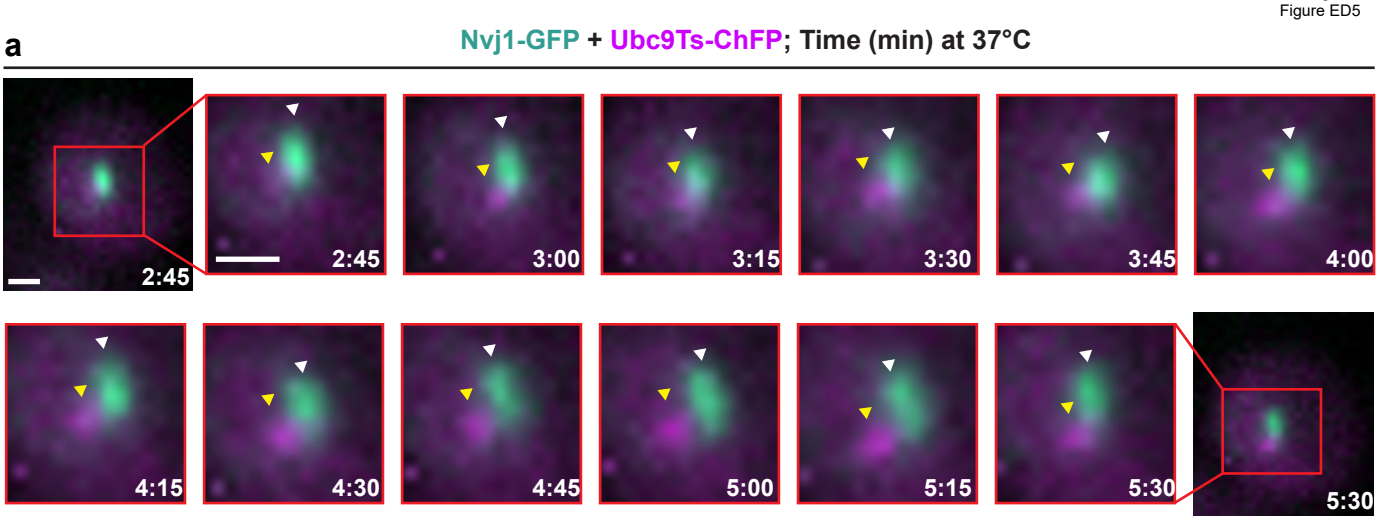

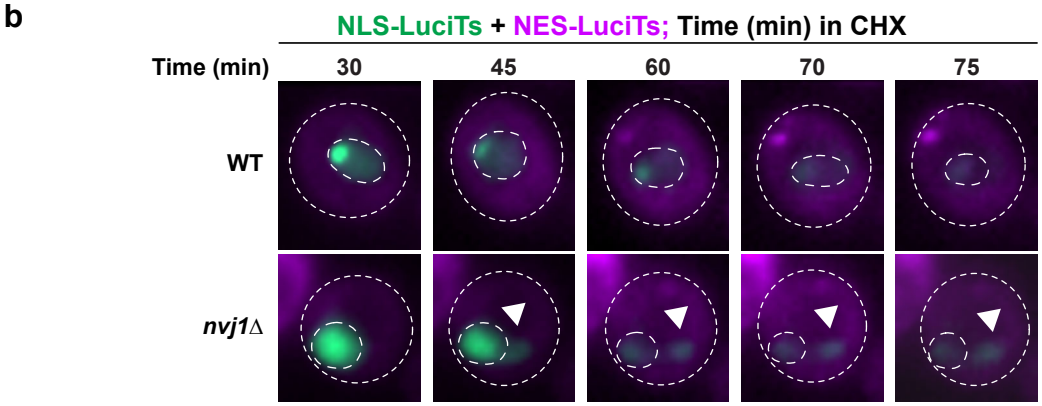

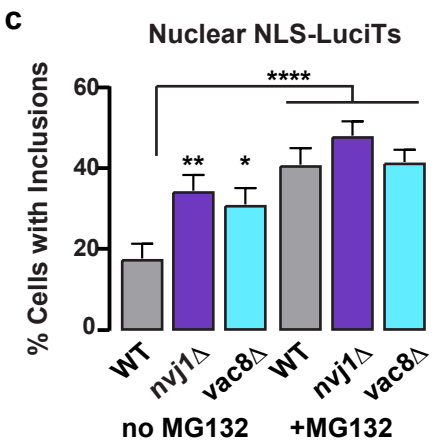

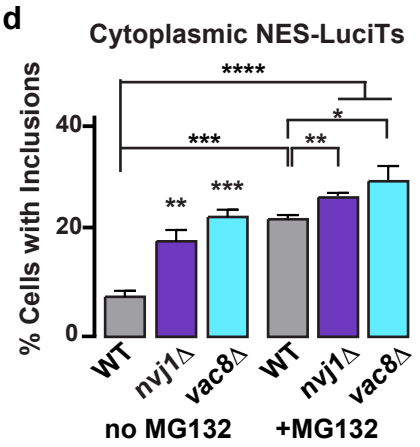

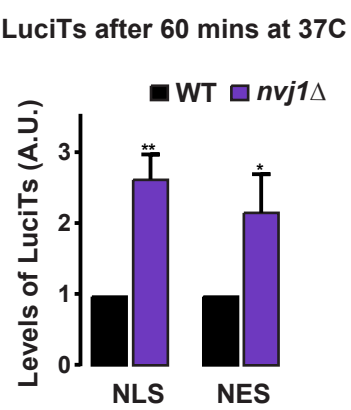

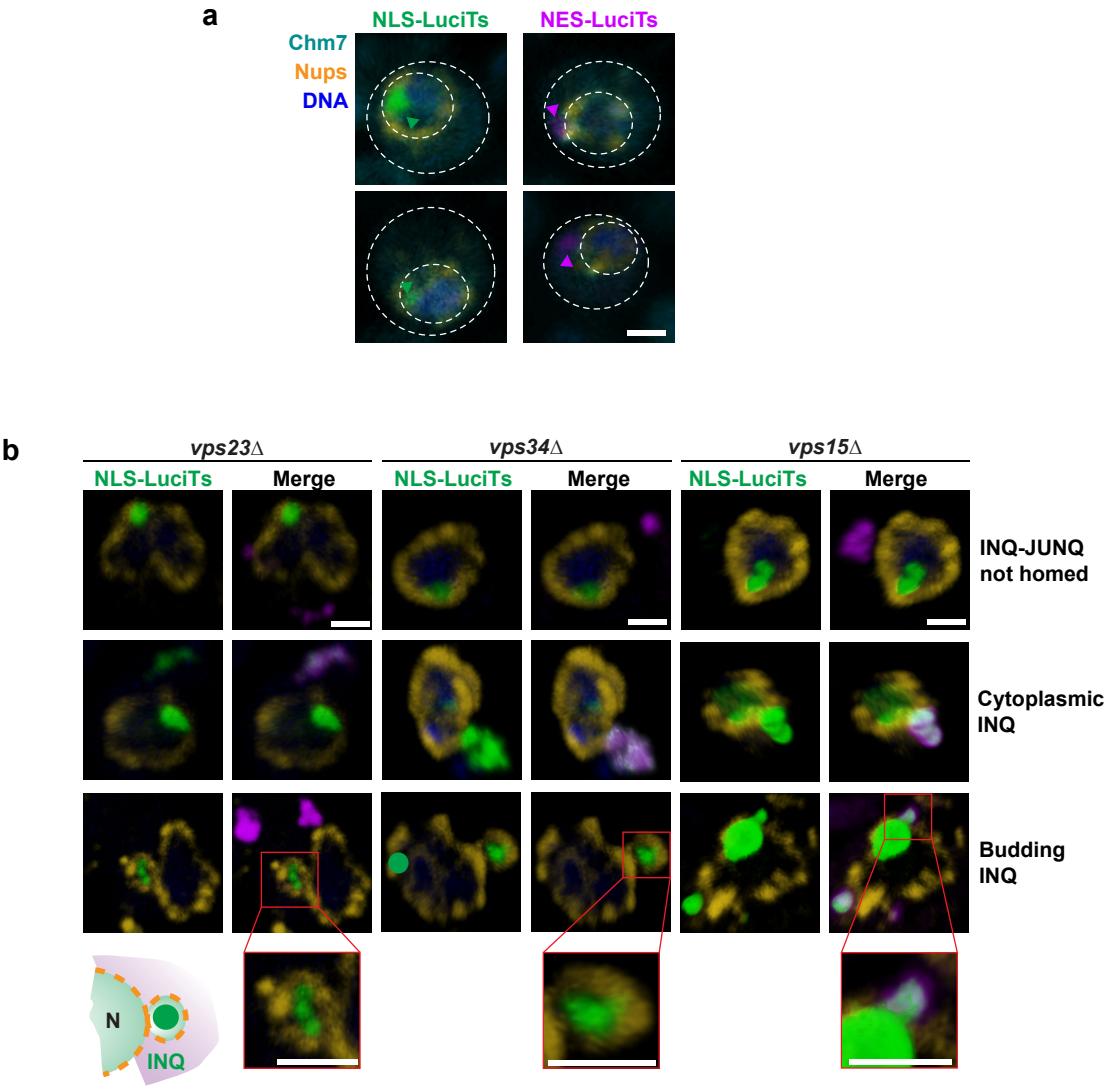
a
NLS-LuciTs
NES-LuciTs
Chm7
Nups
DNA
b
vps23Δ
vps34Δ
vps15Δ
NLS-LuciTs
Merge
NLS-LuciTs
Merge
NLS-LuciTs
Merge
INQ-JUNQ
not homed
Cytoplasmic
INQ
Budding
INQ
N
INQ

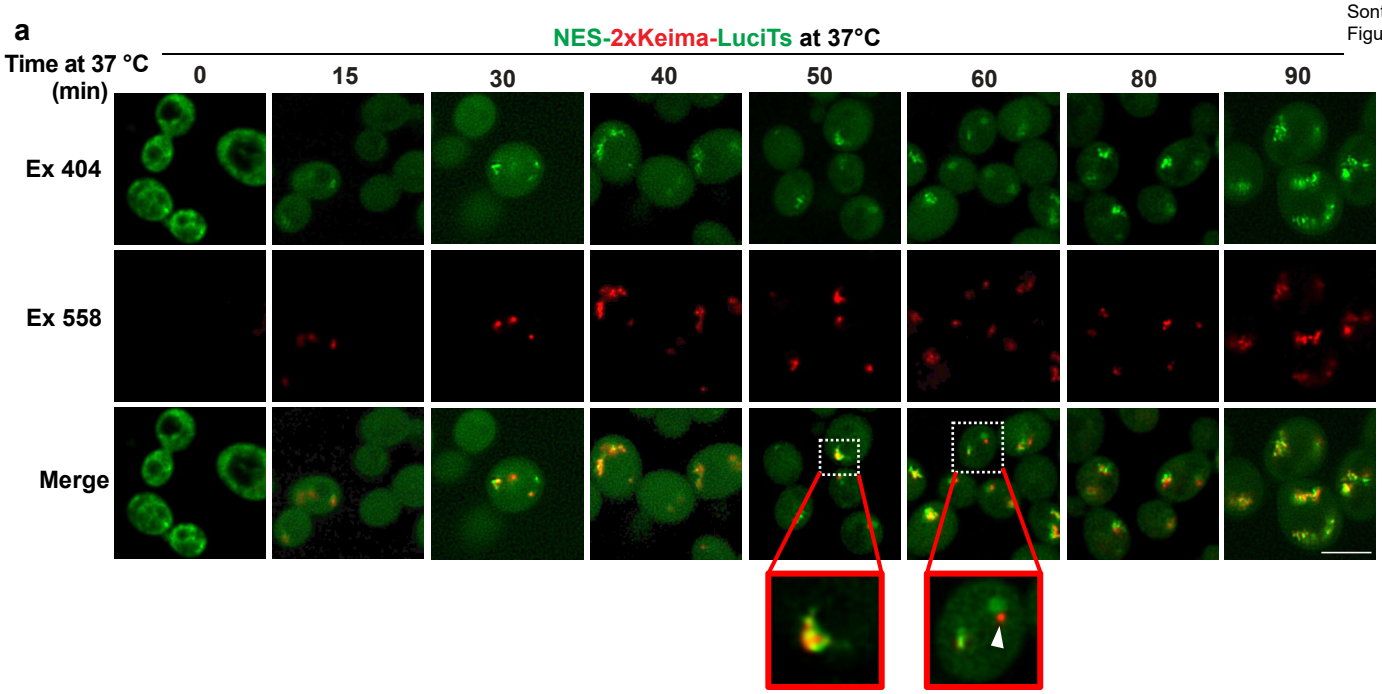
a
NES-2xKeima-LuciTs at 37°C
Time at 37 °C (min)
0
15
30
40
50
60
80
90
Ex 404
Ex 558
Merge

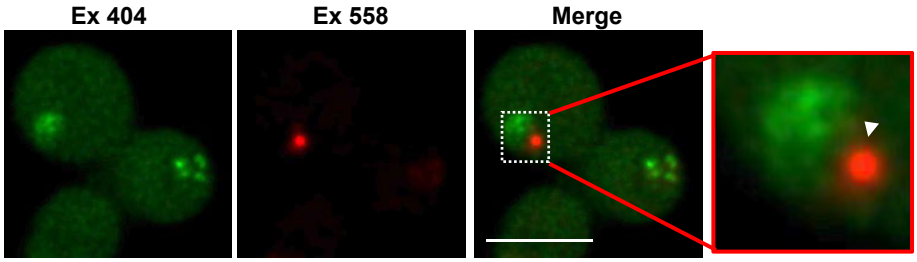
b
NES-2xKeima-LuciTs 85 min chase at 37°C
Ex 404
Ex 558
Merge

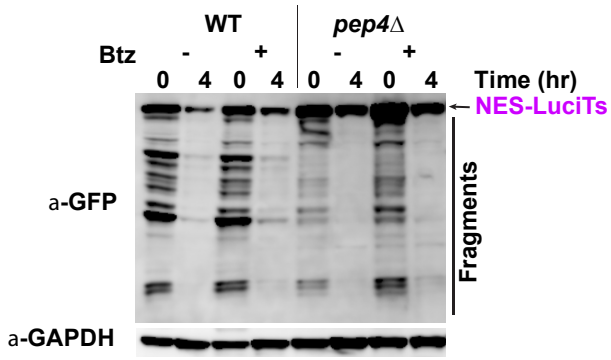
c
WT
pep4Δ
Btz
-
+
-
+
0
4
0
4
0
4
0
4
Time (hr)
NES-LuciTs
Fragments
a-GFP
a-GAPDH

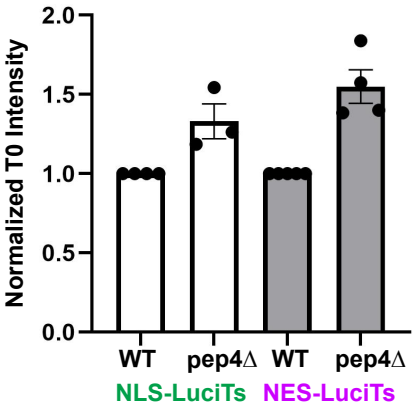
d
Normalized T0 Intensity
2.0
1.5
1.0
0.5
0.0
WT
pep4Δ
WT
pep4Δ
NLS-LuciTs
NES-LuciTs

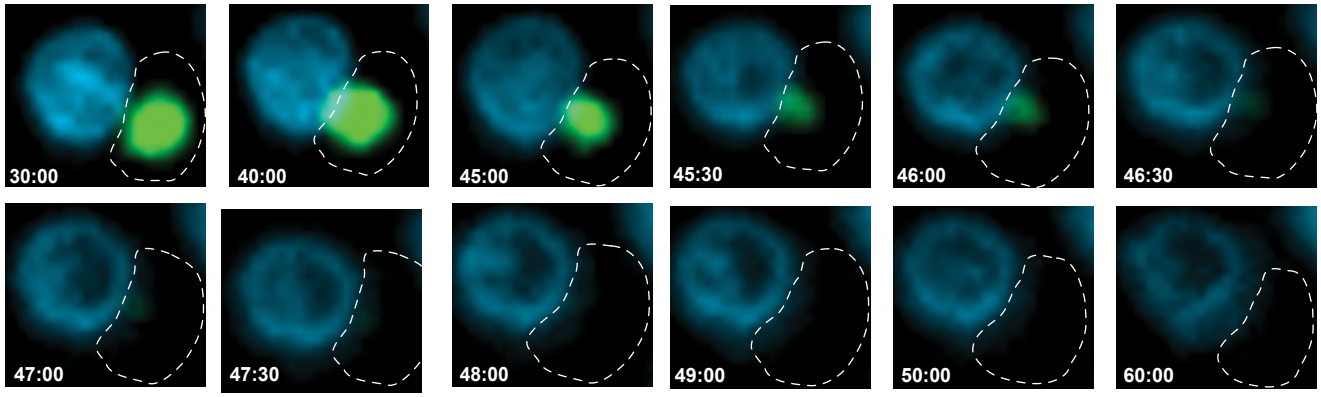
e
WT Chase Time at 37 °C (min)
NLS-LuciTs
Vacuole
30:00
40:00
45:00
45:30
46:00
46:30
47:00
47:30
48:00
49:00
50:00
60:00

SUPPLEMENTARY TABLE S2. Plasmids used in this study		
Nr.	**NAME**	**SOURCE AND COMMENTS**
ES p331	NLS-GFP-LuciTs	This study
ES p357	NES-DsRed-LuciTs	This study
ES p325	NLS-GFP-VHL	This study and (Samant et al. 2018)
ES p355	NES-DsRed-VHL	This study and (Samant et al. 2018)
ES p20	Ubc9Ts-GFP	(Escusa-Toret et al. 2013)
ES p562	Ubc9Ts-ChFP	(Escusa-Toret et al. 2013)
ES p144	GFP-VHL	(Escusa-Toret et al. 2013)
ES p536	pRS NLS-GFP2-NES	(Stade et al., 1997)
ES p57	mHTT 97QP-ChFP	(Escusa-Toret et al. 2013)
ES p520	vt100 GFP	(Westermann et al. 2000)
FMP 1X	NLS-Keima-LuciTs	This study
FMP 1Y	NLS-2xKeima-LuciTs	This study
FMP 2X	NES-Keima-LuciTs	This study
FMP 2Y	NES-2xKeima-LuciTs	This study

SUPPLEMENTARY TABLE S1. Genotypes and sources of yeast strains used in this study				
Nr.	**NAME**	**GENOTYPE**	**SOURCE AND COMMENTS**	
ESY 1	BY4741			
ESY 104	W303			
ESY 105	CRM1		WT strain for crm1-T539C	from Michael Rosbash
ESY 106	crm1-T539C		has nuclear export deficiency with leptomycin B treatment	from Michael Rosbash
ESY 95	Nup116-5	nup116-5::HIS3	SWY027	from Susan Wente
ESY 96	STS1		WT strain for sts1-2	from Kiran Madura
ESY 97	sts1-2		temperature sensitive mutation that blocks proteasome import into the nucleus	from Kiran Madura
ESY 113	*dnm1*	BY4741 Mata	Deletion collection	
ESY 119	*fis1*	BY4741 Mata	Deletion collection	
ESY 122	*fzo1*	BY4741 Mata	Deletion collection	
ESY 123	*ugo1*	BY4741 Mata	Deletion collection	
ESY 121	Mps3-GFP	BY4741 Mata	GFP collection	
ESY 127	*nup120*	BY4741 Mata	Deletion collection	
ESY 94	*nup⊿FG*		SWY3042	from Susan Wente
ESY 14	Nvj1-GFP	BY4741 Mata	GFP collection	
ESY 4	*nvj1*	BY4741 Mata	Deletion collection	
ESY 3	*vac8*	BY4741 Mata	Deletion collection	
ESY 150	*vps4*	BY4741 Mata	Deletion collection	
ESY177	Chm7OPEN-GFP	W303, chm7OPEN-(1-369)-GFP::HIS3	DTCPL413	From Patrick Lusk
ESY183	*Chm7*	W303, chm7Δ::hphMX6		From Patrick Lusk
ESY182	Chm7-GFP	W303, CHM7-GFP::HIS3		From Patrick Lusk
FMP1X	Nvj1-sfGFP	BY4741 Mata	NVJ1 GFP C-terminally tagged	This study